

Review

# A Review: Thermal Stability of Methylammonium Lead Halide Based Perovskite Solar Cells

Tanzila Tasnim Ava, Abdullah Al Mamun, Sylvain Marsillac \*  and Gon Namkoong \*

Department of Electrical and Computer Engineering, Old Dominion University, Applied Research Center, 12050 Jefferson Ave, Newport News, VA 23606, USA; tava001@odu.edu (T.T.A.); amamu001@odu.edu (A.A.M.)

\* Correspondence: smarsill@odu.edu (S.M.); gnamkoon@odu.edu (G.N.); Tel.: +1-757-269-5349 (G.N.)

Received: 29 November 2018; Accepted: 29 December 2018; Published: 7 January 2019



**Featured Application:** solar cells, photodetectors

**Abstract:** Perovskite solar cells have achieved photo-conversion efficiencies greater than 20%, making them a promising candidate as an emerging solar cell technology. While perovskite solar cells are expected to eventually compete with existing silicon-based solar cells on the market, their long-term stability has become a major bottleneck. In particular, perovskite films are found to be very sensitive to external factors such as air, UV light, light soaking, thermal stress and others. Among these stressors, light, oxygen and moisture-induced degradation can be slowed by integrating barrier or interface layers within the device architecture. However, the most representative perovskite absorber material,  $\text{CH}_3\text{NH}_3\text{PbI}_3$  ( $\text{MAPbI}_3$ ), appears to be thermally unstable even in an inert environment. This poses a substantial challenge for solar cell applications because device temperatures can be over 45 °C higher than ambient temperatures when operating under direct sunlight. Herein, recent advances in resolving thermal stability problems are highlighted through literature review. Moreover, the most recent and promising strategies for overcoming thermal degradation are also summarized.

**Keywords:** photovoltaic; perovskite solar cells; thermal decomposition; thermal stability

## 1. Introduction

Increasing global demand for energy and continued reductions in fossil fuel-based energy sources call for the greater use of alternative renewable energy sources. Among the possible renewable sources of energy, solar energy is the most promising, as it can be converted into electrical energy and reach almost every part of the world. Commercially available solar cells are based on silicon, GaAs (gallium arsenide), CdTe (cadmium telluride) and CIGS (copper indium gallium (di)selenide) and have sufficiently established efficiencies to meet global energy demand. However, efforts have been made to reduce the cost [1] of these existing technologies by replacing them with cheaper alternative photovoltaic devices such as perovskite solar cells (PSCs). Currently, the photo-conversion efficiency (PCE) of PSCs has soared beyond 20% in less than five years of laboratory research [2].

Miyasaka, et al. first introduced organic-inorganic hybrid perovskite absorber layer in dye sensitized solar cells (DSSCs) configuration with an efficiency of only 3.81% [3]. The poor stability and efficiency of liquid electrolyte-based structures were attributed to iodine-based redox processes. The efficiency increased to 10% when the liquid electrolyte was replaced with a solid-state hole transport layer of spiro-OMeTAD and led to stability improvements as well [4]. Currently, for PSCs, a planar heterojunction structure (introduced by Snaith, et al. [4]) is widely used, and consists of a solid perovskite layer with electron and hole selective contacts. The planar heterojunction structure can be fabricated at a low temperature (<150 °C), while the mesoporous  $\text{TiO}_2$  scaffold structure requires high temperature (<400 °C), making the former structure superior to the latter structure in terms of cost [5].

The projected theoretical maximum efficiency of solar cells made of this type of device structures is higher than 30%, which would surpass the practical efficiency of ~25% for silicon solar cells [6].

The promising performance of perovskite solar cells has been attributed to extraordinary material properties, including high absorption coefficient, long charge carrier diffusion length, low exciton binding energy, and tunable bandgap [7–12]. However, despite achieving lab-scale device efficiency comparable to that of commercially available solar cells, PSCs retain critical issues regarding stability. Standard PV modules available on the market are typically warranted to retain their initial efficiency for 20–25 years [13]. Since perovskite solar cells are prone to degradation when exposed to air, UV light, thermal stress (heat), light soaking, electric fields, and many other factors [14–16], they cannot currently achieve such a market requirement. Hence, extensive research has recently focused on the study of degradation mechanisms to improve perovskite solar device stability. Stability improvements could be achieved by device encapsulation, adding UV filters, and suppressing trap states for degradation caused by air, UV light, and electric fields, respectively [17–20], but degradation due to thermal stress is considered inevitable since it is difficult to avoid the temperature rise of the solar cells during operation. The effective operational temperature can range from  $-40\text{ }^{\circ}\text{C}$  to  $+85\text{ }^{\circ}\text{C}$  [21], so the standard heat stability test is commonly run within this temperature window.

In this review paper, we aim to present a survey of the existing literature on the thermal stability of the most commonly used methyl ammonium halide perovskite solar cells. We will first focus on the evolution of the structural stability of perovskite materials, followed by the impact of thermal stress on perovskite solar devices. Perovskite solar cells consist of many layers and this study specifically highlights the intrinsic degradation mechanisms of the perovskite absorber layer, including chemical, morphological, and optical degradation. In addition, the effect of thermal stress on other layers in the device architecture has also been reviewed, particularly noting the degradation of charge transport layers and metal contacts, and presents solutions to slow down the degradation. Finally, the available strategies to improve the thermal stability of perovskite solar cells are depicted.

## 2. Structural Stability of Perovskite

The structural stability of the perovskites is critical when used in photovoltaic devices, since they are expected to remain stable for more than 25 years [22]. Structural stability is defined as the ability for a crystalline phase to be stable over a wide range of external factors such as heat, pressure, moisture, etc. Perovskite compounds have a general chemical formula of  $\text{ABX}_3$ , where A and B are cations and X is an anion. Their crystal structure is similar to that of calcium titanium oxide. Usually, the A cations are larger than the B cations. Oxide perovskites have been studied extensively because of their multifunctional nature [23]. However, owing to their wide bandgap, oxide perovskites harvest only 8–20% of the solar spectrum, limiting their use in photovoltaic applications [23]. Instead, halide organic-inorganic perovskites were developed by replacing the oxygen anion of oxide perovskites with an inorganic halide ( $\text{I}^-$ ,  $\text{Cl}^-$ ,  $\text{Br}^-$ ) [23]. An organic or inorganic monovalent  $\text{A}^+$  cation (e.g.,  $\text{Rb}^+$ ,  $\text{Cs}^+$ ,  $\text{CH}_3\text{NH}_3^+$ ,  $\text{HC}(\text{NH}_2)_2^+$ ) and a divalent  $\text{B}^{2+}$  metal cation (e.g.,  $\text{Pb}^{2+}$ ,  $\text{Sn}^{2+}$ ) were also implemented in the frame of the perovskite structures [23]. The halide perovskites obtain a desired crystal symmetry by maintaining an allowable tolerance factor. A tolerance factor developed by Goldschmidt [24] determines the radii sizes associated with cubic symmetry, described by

$$t = \frac{R_A + R_X}{\sqrt{2}(R_B + R_X)} \quad (1)$$

where  $R_A$ ,  $R_B$ ,  $R_X$  are the ionic radii of A, B, X, respectively. The tolerance factor provides a rough estimate of the stability and distortion of crystal structures of a compound. In addition, it gives an idea of whether the phase is cubic ( $t = 1$ ) or deviates into the tetragonal or orthorhombic phase [25]. In general, an established tolerance factor value for halide perovskites lies in the range of  $0.85 < t < 1.11$  [26]. Non-perovskite structures are formed when the tolerance factor is higher or lower. In an inorganic-organic hybrid perovskite, it is difficult to calculate the absolute tolerance factor as the

organic cation has a non-spherical geometry [27]. However, it is possible to qualitatively analyze the transition of structure in these materials. For example, formamidinium lead iodide,  $\text{HC}(\text{NH}_2)_2\text{PbI}_3$  (FAPbI<sub>3</sub>), has a larger A cation than methylammonium lead iodide,  $\text{CH}_3\text{NH}_3\text{PbI}_3$  (MAPbI<sub>3</sub>) and a larger cation would generally represent a higher tolerance factor [28]. Two phases can be obtained in solution-processed FAPbI<sub>3</sub> materials. One is the photoactive  $\alpha$ -phase (black phase) and the other is a non-photoactive phase (yellow phase or  $\delta$ -phase) [29].

Figure 1a,b shows the ideal case of cubic symmetry for perovskites. The cubic symmetry corresponds to a  $Pm\bar{3}m$  space group with 12-fold coordination for the A cation, 6-fold coordination for the B cations, and  $\text{BX}_6$  octahedra residing in the corners [23]. The deviation from cubic symmetry can be attributed to several factors including the atomic sizes of the constituents. The A cation does not directly affect the electronic properties [30–32]; however, the size of A cations can cause distortion of the B-X bonds, which undesirably affects the symmetry. The best electronic properties are obtained with cubic symmetry due to high ionic bonding. An octahedral tilting occurs when the tolerance factor exceeds the ideal range, and affects the electronic properties.

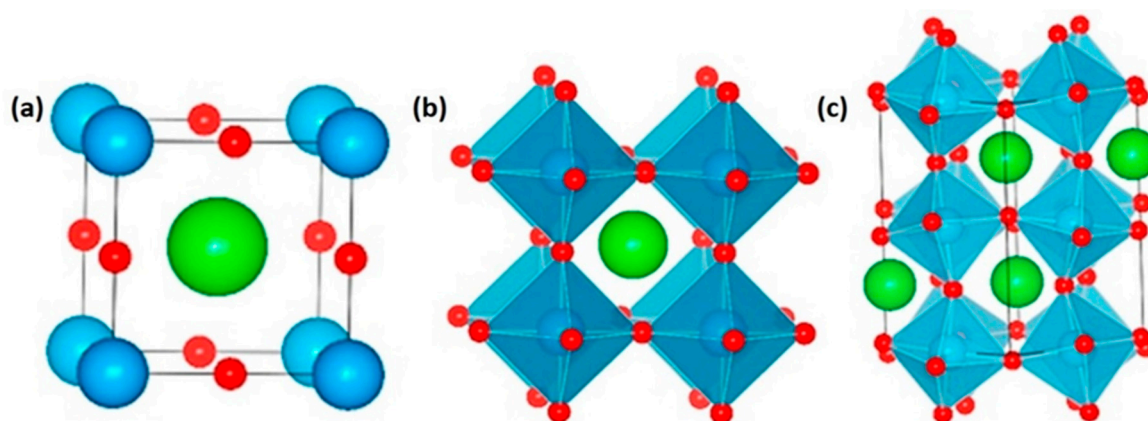


**Figure 1.** (a) The unit cell of cubic perovskite, where the blue spheres at lattice corners are A cations, the green sphere at the center is a B cation, and the red spheres at the lattice faces are X anions. (b) Another illustration of  $\text{BX}_6$  octahedral network, where B cations are surrounded by X anions. (c) A tilted  $\text{BX}_6$  octahedral structure due to non-ideal size effects and additional factors. Reprinted from [23], with permission from Elsevier.

In recent years, methylammonium lead trihalide ( $\text{MAPbX}_3$ ) has received increasing attention as an absorber material for perovskite solar cells. However, the stability of  $\text{MAPbX}_3$  has been found to strongly vary depending on temperature, changing phase or crystal orientation. The structural data of various methylammonium lead trihalides ( $\text{MAPbX}_3$ ; X = I, Cl, Br) [33,34] are summarized in Table 1. As indicated in Table 1, both  $\text{MAPbBr}_3$  and  $\text{MAPbCl}_3$  crystallize in the cubic phase at room temperature, while  $\text{MAPbI}_3$  needs to be heated to a temperature higher than 323 K to allow the transition from a tetragonal to a cubic phase. Interestingly, many studies on  $\text{MAPbI}_3$  materials report that the tetragonal phase of  $\text{MAPbI}_3$  can still exist even after heating at temperature of 373 K [4,35–37]. This suggests that the tetragonal phase is surprisingly stable in the thin films, but also emphasizes an ambiguity about the exact phase transition temperature and the nature of the phase transition between tetragonal and cubic phases.

**Table 1.** Structural data for various methylammonium lead trihalides [22].

Halides (X)	Temperature (K)	Crystal Structure	Space Group	Lattice Parameter (Å)		
				a	b	c
Cl	>178.8	Cubic	<i>Pm3m</i>	5.675		
	172.9–178.8	Tetragonal	<i>P4/mmm</i>	5.656		5.630
	<172.9	Orthorhombic	<i>P222<sub>1</sub></i>	5.673	5.628	11.182
Br	>236.9	Cubic	<i>Pm3m</i>	5.901		
	155.1–236.9	Tetragonal	<i>I4/mcm</i>	8.322		11.832
	149.5–155.1	Tetragonal	<i>P4/mmm</i>	5.894		5.861
	<144.5	Orthorhombic	<i>Pna2<sub>1</sub></i>	7.979	8.580	11.849
I	>327.4	Cubic	<i>Pm3m</i>	6.329		
	162.2–327.4	Tetragonal	<i>I4/mcm</i>	8.855		12.659
	<162.2	Orthorhombic	<i>Pna2<sub>1</sub></i>	8.861	8.581	12.620

### 3. Impact of Thermal Stress on Perovskites

Typically, device temperatures can be over 45 °C higher than ambient temperatures when solar cells operate under direct sunlight. According to International Standards (IEC 61646 climatic chamber tests), long-term stability at 85 °C is required to compete with other solar cell technologies [38]. Therefore, the study of the thermal stability of perovskite solar devices has attracted world-wide research attention. Different degradation pathways have been proposed and the topic remains under discussion, but the material MAPbI<sub>3</sub> (CH<sub>3</sub>NH<sub>3</sub>PbI<sub>3</sub>) clearly loses its excellent light harvesting properties over time because it evolves into PbI<sub>2</sub> after a nominal loss of CH<sub>3</sub>NH<sub>3</sub>I. The degradation from CH<sub>3</sub>NH<sub>3</sub>PbI<sub>3</sub> to PbI<sub>2</sub> is most likely accompanied by a release of gases via simple sublimation or assisted chemical reaction. It is proposed that the first mass loss step during the thermal degradation of CH<sub>3</sub>NH<sub>3</sub>PbI<sub>3</sub> and CH<sub>3</sub>NH<sub>3</sub>I under an inert atmosphere proceeds as [39]:



Therefore, the determination of the composition of these released gases during the controlled thermal degradation of CH<sub>3</sub>NH<sub>3</sub>PbI<sub>3</sub> is expected to pinpoint the degradation pathways. Different interpretations can be found in the literature regarding the chemical nature of these released gases during thermal degradation and several studies have analyzed the effect of intrinsic degradation and thermal stress on the perovskites. Herein, an overview of the impact of thermal stress on perovskites, based on different aspects such as chemical, crystallographic, morphological and optical degradation, is described.

#### 3.1. Chemical and Structural Degradation

Fan, et al. [40] studied the thermal degradation of MAPbI<sub>3</sub> by fabricating MAPbI<sub>3</sub> microplates. Microplates are highly crystalline and thus provide an outstanding opportunity to study the structural degradation mechanisms of perovskites. The authors investigated the crystal structure under thermal stimulation using in-situ high-resolution transmission electron microscopy (HRTEM). They found that almost 75% of the original perovskite tetragonal phase returned to trigonal PbI<sub>2</sub> after 100 s of heating at 85 °C. Degradation is initiated by breaking the weak Pb-I-Pb bond along the (001) direction [41], after which the PbI<sub>2</sub> relaxes into its energetically favorable trigonal structure (Figure 2). During this process, CH<sub>3</sub>NH<sub>2</sub> and HI sublime into the gas phase. Their studies conducted in dry and inert gaseous environments revealed that no MAPbI<sub>3</sub> hydrates are generated during the degradation process [42–44]. The authors therefore concluded that the phase transition to PbI<sub>2</sub> is not initiated by the intrinsic hygroscopicity of alkylammonium cations [38,44], but instead is completely due to the thermally induced degradation. They suggested that a sequential transition occurs from tetragonal MAPbI<sub>3</sub>

to trigonal  $\text{PbI}_2$  based on the time-dependent studies, which showed an overlap of the  $\text{MAPbI}_3$  and  $\text{PbI}_2$  crystal structures in the electron diffraction patterns under thermal stress. In particular, the diffraction intensity of the perovskite tetragonal phase was correlated with a direct increase in the  $\text{PbI}_2$  trigonal phase intensity. This correlation indicates that the structure is a stacked architecture, with  $\text{PbI}_2$  formed on top of the underlying  $\text{MAPbI}_3$  layers. In addition, the thickness of each layer varies with the annealing time, with the thermal transformation from  $\text{MAPbI}_3$  to  $\text{PbI}_2$  occurring through bulk or surface reactions. To understand the actual reaction process, they conducted density functional theory (DFT) calculations [44]. The corresponding reaction rate calculated for the minimum energy path from  $\text{MAPbI}_3$  to  $\text{PbI}_2$  through bulk degradation was found to be approximately 1000 times slower than surface-initiated decomposition [44]. Therefore, they concluded that surface degradation is kinetically preferred. The first layer is degraded, and the underlying layer gets exposed. The process is repeated until the entire material degrades, which supports the theory that it is a surface-dominated reaction [44].

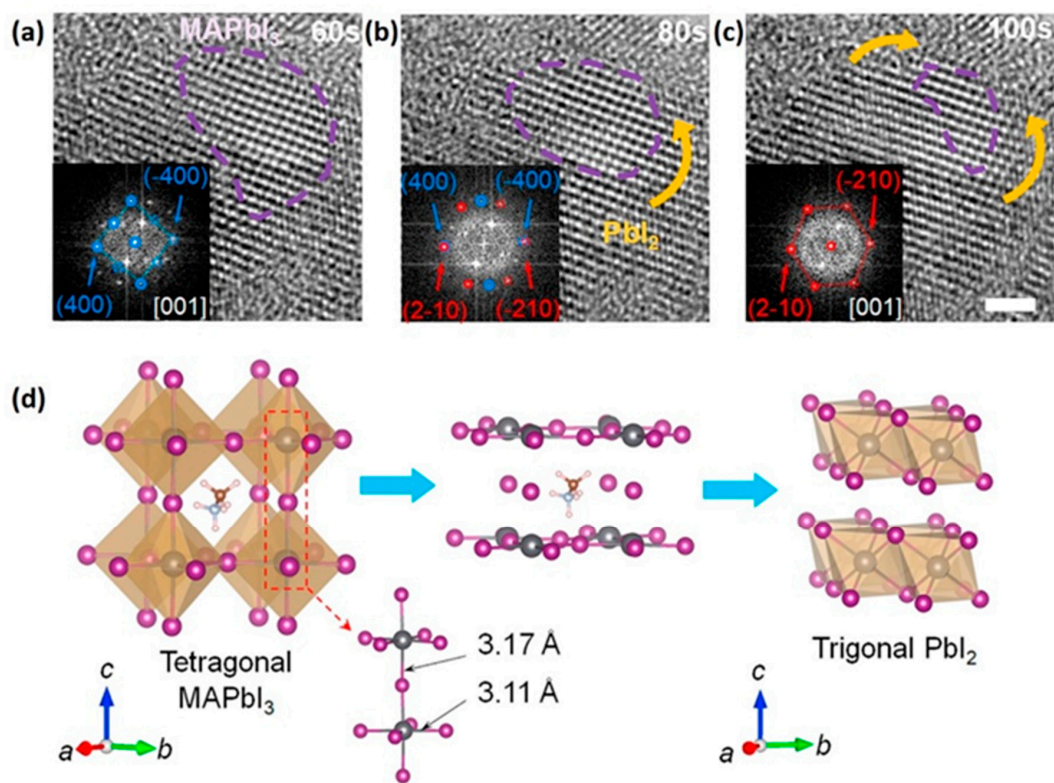


**Figure 2.** (a–c) Degradation process of  $\text{MAPbI}_3$  grain with direct transition from tetragonal to trigonal crystalline structure. The purple dashed lines in (a–c) showed the shrinking of perovskite and the insets represented Fast Fourier transform (FFT) phase diagrams of the corresponding HRTEM images (Scale bar = 2 nm). (d) Transition from  $\text{MAPbI}_3$  with a tetragonal configuration to  $\text{PbI}_2$  with a trigonal configuration. Reprinted from [40], with permission from Elsevier.

The thermal stability of perovskite solar cells, with a structure of  $\text{ITO}/\text{TiO}_2/\text{MAPbI}_3$ , was studied by Conings and co-workers [38]. In order to separate the perovskite layer degradation from degradation at other interfaces, the hole transfer layer (HTL) and the top electrode were excluded. The samples were heated at  $85^\circ\text{C}$  for 24 h, under four environmental conditions: pristine film (reference),  $\text{O}_2$  environment,  $\text{N}_2$  environment and ambient conditions. The X-ray diffraction (XRD) patterns revealed the formation of  $\text{PbI}_2$  under ambient conditions, as shown in Figure 3a. Smecca, et al. [45] showed that the peak at  $2\theta = 14.00^\circ$  (corresponding to a unique (001) plane of  $\text{MAPbI}_3$ ) decreased along with an increase of the peak at  $2\theta = 12.61^\circ$  (corresponding to a (003) plane of  $\text{PbI}_2$ ) (Figure 3b,c).

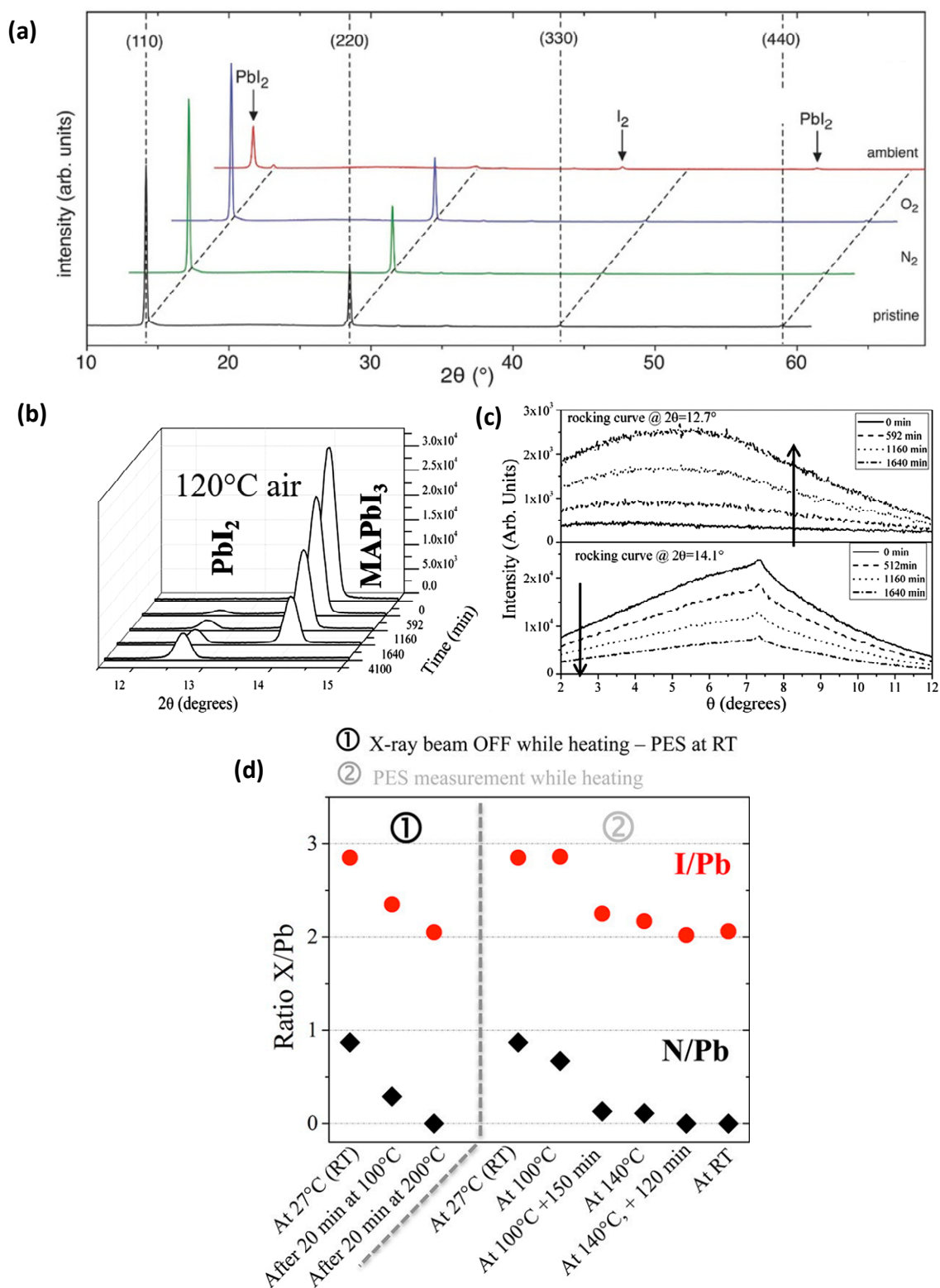


**Figure 3.** (a) XRD patterns of ITO/TiO<sub>2</sub>/perovskite samples heated at 85 °C for 24 h in different atmospheres. Reprinted with permission from [38]. (b) XRD patterns of MAPbI<sub>3</sub> film collected at 120 °C in air at different times and (c) the corresponding rocking curves at  $2\theta = 14.11^\circ$  and  $2\theta = 12.71^\circ$ . Reprinted with permission from [45]. (d) The atomic ratio of I/Pb (red circle) and N/Pb (black diamond) at elevated temperatures analyzed from photoelectron spectroscopy measurement. Reprinted with permission from [46]. Copyright (2015) American Chemical Society.

All peaks related to the perovskite layer disappeared in the diffraction pattern during thermal annealing. On the basis of these findings, the authors concluded that the perovskite layer degraded into  $\text{PbI}_2$  in less than 10 h. Similarly, Phillippe and co-workers investigated the effect of higher temperatures on both  $\text{MAPbI}_3$  and  $\text{MAPbI}_{3-x}\text{Cl}_x$  films [46], but used hard X-ray photoelectron spectroscopy (HX-PES) instead of XRD in their study. HX-PES aids the understanding of the film decomposition procedure by determining the chemical composition of the sample regardless of crystallinity. To investigate the decomposition process, the samples were prepared in an oxygen- and water-free environment and were heated in an analysis chamber under ultra-high vacuum. The films were quantitatively analyzed using HX-PES by extracting the I/Pb and N/Pb atomic ratios. The reduction in these ratios represents the conversion of perovskite to  $\text{PbI}_2$ . The atomic ratio of I/Pb (red circle) and N/Pb (black diamond) plotted at various temperatures are shown in Figure 3d. Heating at 100 °C for 20 min significantly reduced both ratios. Furthermore, upon heating at 200 °C, the two ratios decreased to 2 and 0, respectively. This indicates that the film decomposed completely into  $\text{PbI}_2$ .

### 3.2. Morphological Degradation

Several reports have investigated the effect of temperature on the morphology of perovskites. As mentioned above, Conings and co-workers [38] studied the thermal stability of perovskite solar cells with an ITO/ $\text{TiO}_2$ /MAPbI<sub>3</sub> structure when subjected to heat treatment at 85 °C for 24 h under various environmental conditions. High-angle annular dark field (HAADF) TEM was used to understand the effect of temperature on devices in different environmental conditions. Cross-sectional views of the HAADF images are shown in Figure 4a,b. The pristine perovskite device exhibited well-defined layers stacked evenly on top of each other, while the degraded samples exhibited structural variations. Interestingly, a large  $\text{PbI}_2$  grain, highlighted in red, is formed in the  $\text{O}_2$  environment (see Figure 4c). The calculated ratio of Pb/I determined by EDX revealed the highlighted oblong structure to be  $\text{PbI}_2$ . When exposed to ambient atmosphere, more severe device degradation occurred with spot-like structures in the perovskite and delamination from the  $\text{TiO}_2$  layer, as shown in Figure 4d. Additionally, topographical AFM images (Figure 4e–h) showed significant structural changes for samples measured under ambient conditions. Significant dark areas appearing in AFM images were associated with  $\text{PbI}_2$  regions, which indicates a photocurrent reduction in those regions upon degradation.

Han et al. [17] tested the stability of perovskite solar devices in an environmental chamber, where the temperature was controlled in the range of −20 °C to 100 °C. The actual cell temperature inside the chamber was found to be approximately 30 °C higher than the environmental temperature, so the temperatures were denoted as “environmental temperature (actual cell temperature)”, e.g., 55 °C (85 °C) [17]. The degradation mechanism of  $\text{CH}_3\text{NH}_3\text{PbI}_3$  solar cells was analyzed for 500 h at 55 °C (85 °C) using cross-sectional focused ion beam–scanning electron microscopy (FIB-SEM). The cross-sectional FIB-SEM images shown in Figure 5 reveal the degradation mechanism of an encapsulated device. The direct exposure equivalent to one sun illumination clearly damaged the entire device, with the most degradation observed in the silver layer. A number of degradation features were observed in the degraded cells; including degradation of the silver layer, formation of voids in spiro-OMeTAD and the perovskite layer, and delamination of the perovskite layer from the  $\text{TiO}_2$  layer, as shown in Figure 5a–c. Particularly, the formation of a  $\text{PbI}_2$  layer was found, as indicated by a bright contrast in the SEM image (see Figure 5d). It is anticipated that the degradation was initiated by the reaction of HI gas and Ag in an encapsulated device structure. Therefore, the authors suggested replacing the silver contact and using highly heat-resistant encapsulating materials.

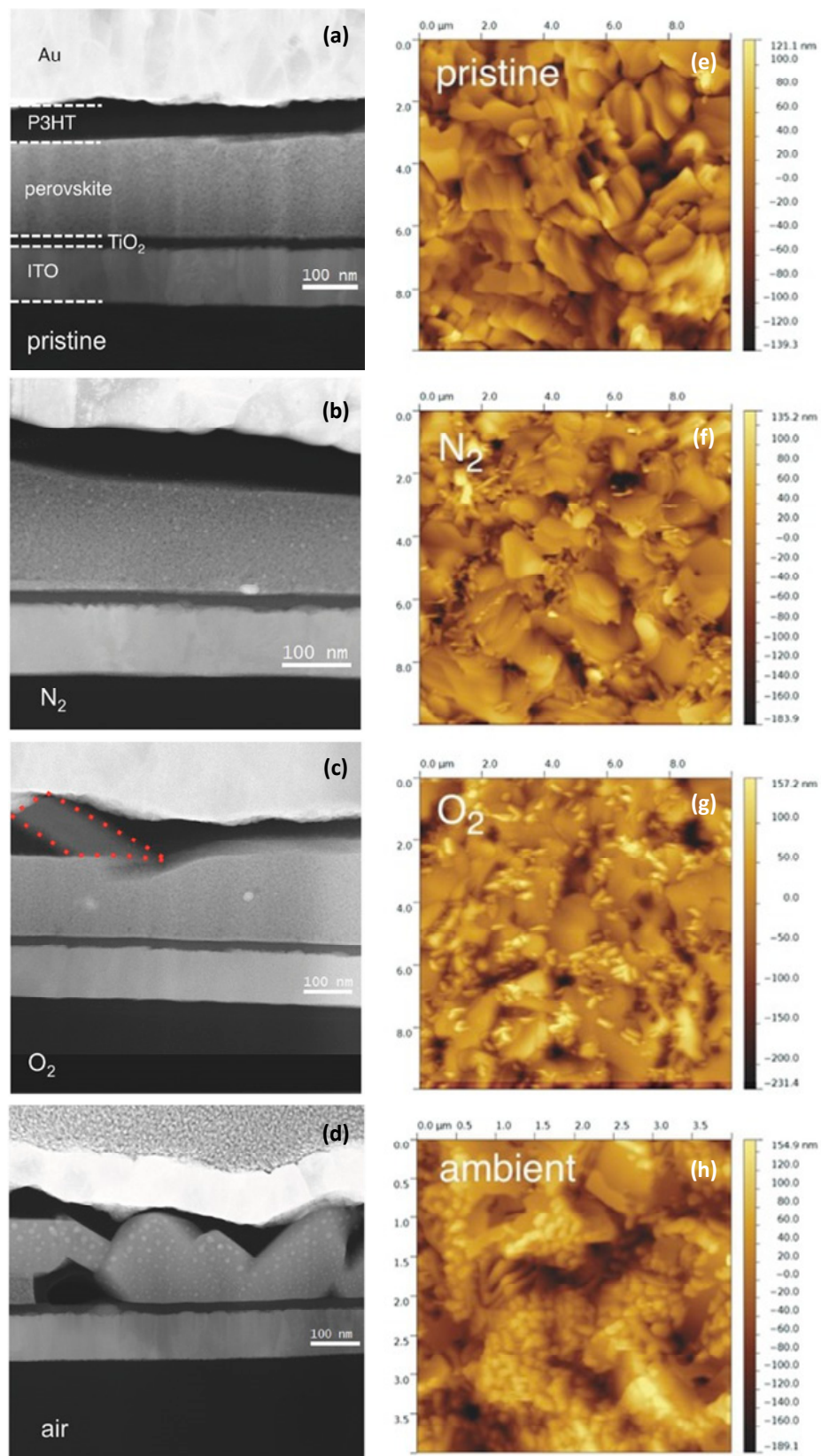


**Figure 4.** (a–d) Cross-sectional views of perovskite solar cells heated at 85 °C for 24 h in different atmospheric conditions. The area highlighted in red in the degraded device in O<sub>2</sub> environment indicates the presence of PbI<sub>2</sub> grain. (e–h) Topographical AFM images of perovskite films that were heated at 85 °C for 24 h in different atmospheric conditions. Reprinted from [38] with permission.

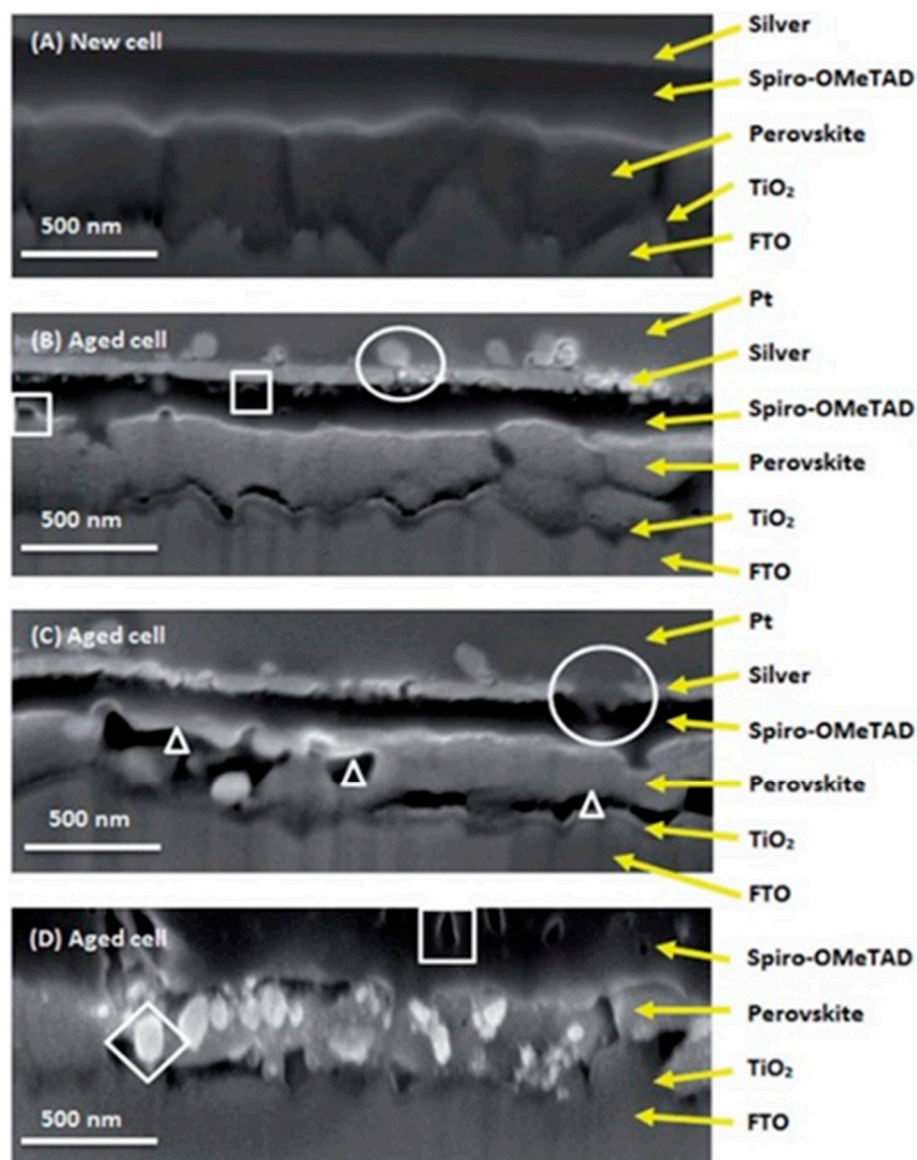


**Figure 5.** Cross-sectional FIB-SEM images of a (A) (a) A fresh cell and (b-d) cells aged at high temperature (55 °C (85 °C)) and humidity (50%) for 500 h. Degradations in different layers are denoted as voids in the Spiro-OMeTAD layer (□); voids in the perovskite layer (Δ); degraded silver layer (○) and formation of particles with higher atomic numbers, likely PbI<sub>2</sub> (◇). Reprinted with permission from [17].

### 3.3. Optical Degradation

Foley et al. [47] investigated the temperature dependence of the bandgap and energy levels of MAPbI<sub>3</sub> by employing absorbance and photoluminescence (PL) spectroscopy (Figure 6a,b). They showed that both valence band maximum (VBM) and conduction band minimum (CBM) levels were reduced by 110 meV and 77 meV, respectively, when the temperature was increased from 25 °C to 85 °C. The bandgap of MAPbI<sub>3</sub> also increased by 33 meV, with an increase in temperature. This provided deeper insights into the relationship between the observed shift in VBM level and thermal expansion of the lattice using density functional theory (DFT) calculations. These results are significant when designing MAPbI<sub>3</sub> solar cells at different operating temperatures. Recently, the effects of heating and cooling on the performance of MAPbI<sub>3-x</sub>Cl<sub>x</sub> perovskite solar cells were investigated by varying the device temperatures from room temperature to 82 °C and then returning them to room temperature [48]. For this study, temperature-dependent steady-state PL and time-resolved lifetime decay measurements

were investigated using a Linkam THM S600E system. Interestingly, an irreversible optical and electrical degradation of the perovskite films was observed at 70 °C. This irreversible degradation continued up to 82 °C and even when the device was cooled back to below 82 °C. PL measurements, shown in Figure 6c,d, demonstrate this irreversible degradation. An increase in the disordered phase of the perovskite films (observed by PL measurements) was found to result in a drastic increase in charge trapping and the development of a deeper trap depth. Temperature-dependent lifetime decay measurements were performed and the trapping and detrapping rates were calculated [48] to show a trap depth of 145 meV for temperatures in the range 40–70 °C. However, a deeper trap depth of 1.1 eV was observed at temperatures over 70 °C, indicating the formation of deep trap states due to the thermal decomposition of the perovskite layer (Figure 6e,f). Herz et al. also observed a gradual shift in the band-edge of MAPbI<sub>3</sub> at elevated temperature (100 °C) based on PL and transmittance measurements [49]. These results suggest that the observed intrinsic thermal decomposition of perovskite solar cells at such low temperatures may limit their commercial applications.

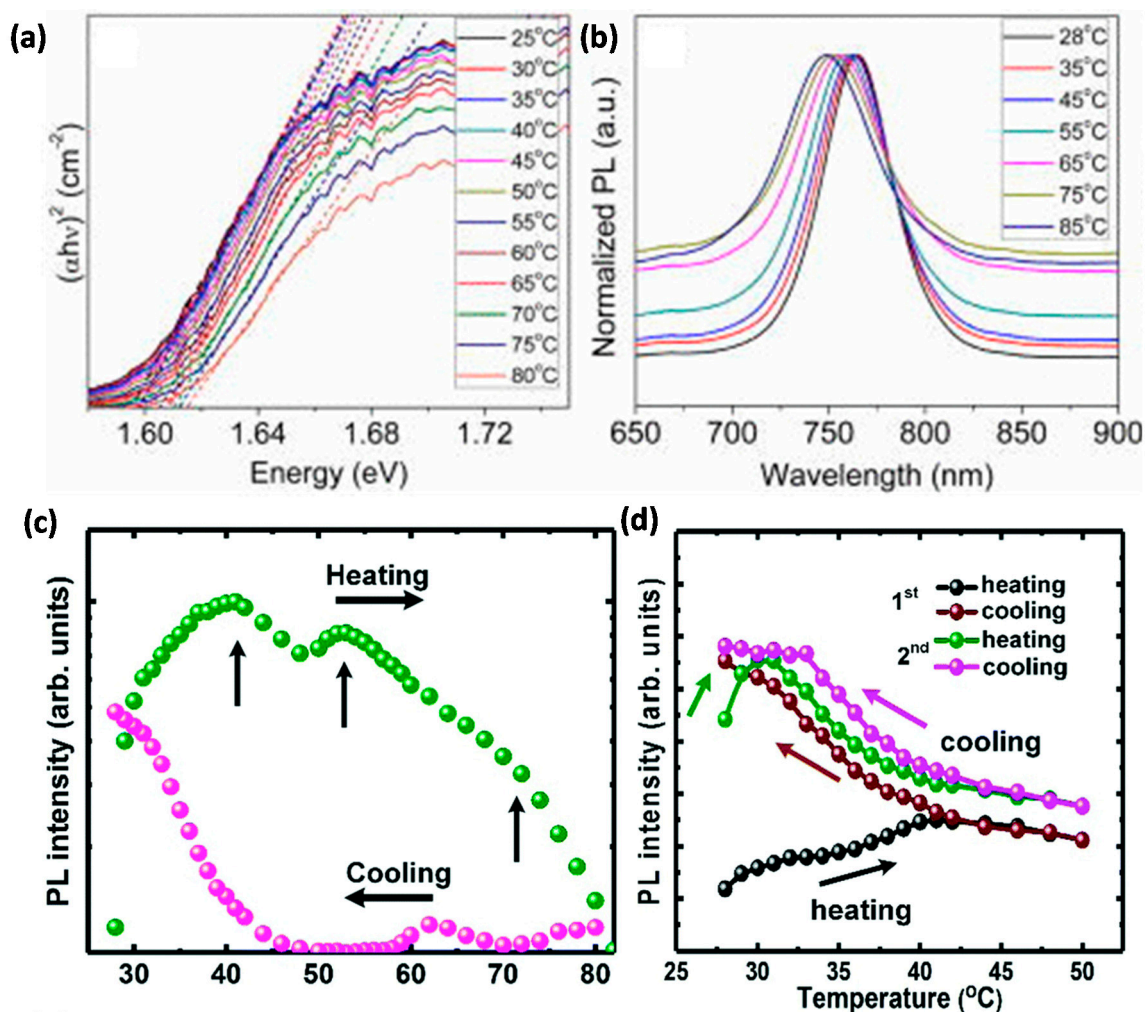
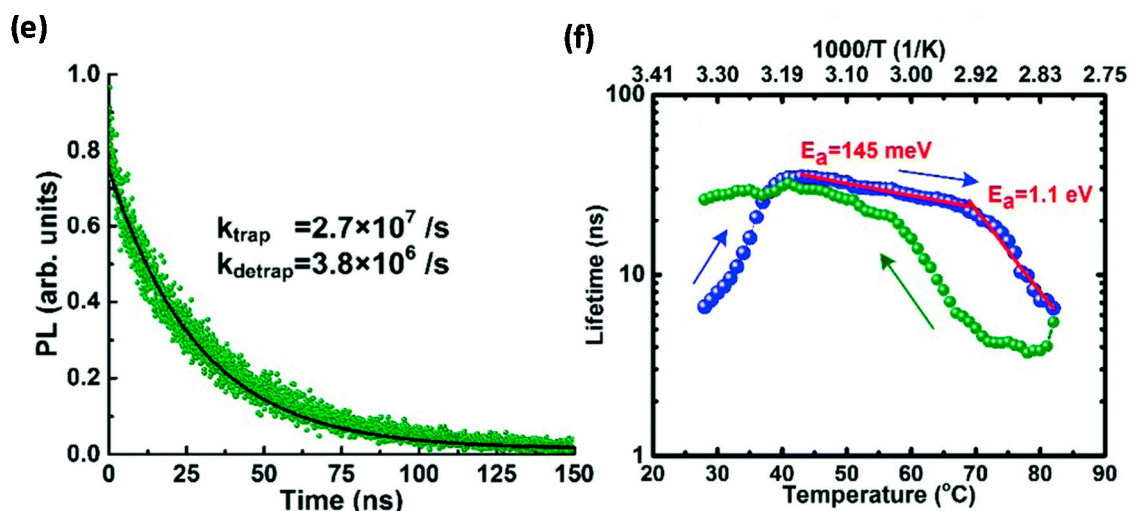


Figure 6. Cont.



**Figure 6.** Temperature dependent (a) absorbance and (b) photoluminescence spectra of MAPbI<sub>3</sub> when the temperature is increased from 28 °C to 85 °C. Reprinted with permission from [47]. (c) photoluminescence (PL) intensity plotted as a function of temperature showing three transitional PL peaks during the heating process. (d) PL measurements as a function of temperature during the heating and cooling processes (room temperature to 52 °C). (e) Best-fit of lifetime decay using trapping and detrapping model. (f) Evolution of the lifetime of MAPbI<sub>3-x</sub>Cl<sub>x</sub> during heating and cooling processes. The trap depths of 145 meV for temperatures in the range 40–70 °C and 1.1 eV above 70 °C were obtained from a quantitative analysis of the Arrhenius plots. Reprinted with permission from [48].

#### 4. Impact of Thermal Stress on Various Layers and Possible Solutions

We now move the stability discussion to the other important layers of perovskite solar cells. In particular, we will discuss how the temperature affects the electron transport layer (ETL), the hole transport layer (HTL), and the metal electrode.

##### 4.1. Electron Transport Layers

The most commonly used ETL in perovskite solar devices is titanium dioxide (TiO<sub>2</sub>). However, non-stoichiometric defects, such as oxygen vacancies and titanium interstitials, can also form in this layer [50] and cause deep sub-band gap trap states. Perovskite devices with TiO<sub>2</sub> ETL show rapid degradation under illumination. Recently, Ahn et al. reported the degradation of the photo conversion efficiency of perovskite solar cells due to the decomposition of the perovskite film at the interface with TiO<sub>2</sub> [51]. As shown by the SEM images, degradation is initiated at the perovskite/TiO<sub>2</sub> interface in a TiO<sub>2</sub>-based device. The authors postulated that the trapped charges at the interface were responsible for the irreversible degradation of perovskites along grain boundaries [51]. To enhance stability, compact TiO<sub>2</sub> ETL can be replaced with C<sub>60</sub>, which shows much more stable performance when deployed in the device structure.

Wojciechowski et al. used C<sub>60</sub> as interface modification layer for TiO<sub>2</sub> and as an electron-accepting layer [52,53]. They performed steady-state PL measurements over time at the PL peak of 775 nm in the devices with TiO<sub>2</sub> and C<sub>60</sub> as ETLs (See Figure 7a,b) [53]. The C<sub>60</sub> layer was shown to increase the photoluminescence decay and exhibited more stable device performance under full-spectrum illumination for 500 h, as shown in Figure 7c [53]. The control device with TiO<sub>2</sub> as an n-type layer showed a notable reduction in the photovoltaic performance with time as shown in Figure 7d, while the C<sub>60</sub> based device exhibited much more stable performance when annealed at 60 °C for 500 h. To overcome the non-stoichiometric defects of TiO<sub>2</sub>, Pathak et al. [50] used Al-doping for their TiO<sub>2</sub>, and developed a sol-gel deposition process with an Al-containing precursor. Photo-thermal deflection spectroscopy (PDS) measurements indicated that Al-doping in TiO<sub>2</sub> reduced the number of trap states

and they found that Al-doping not only passivated non-stoichiometric defects but also improved the stability of encapsulated devices.

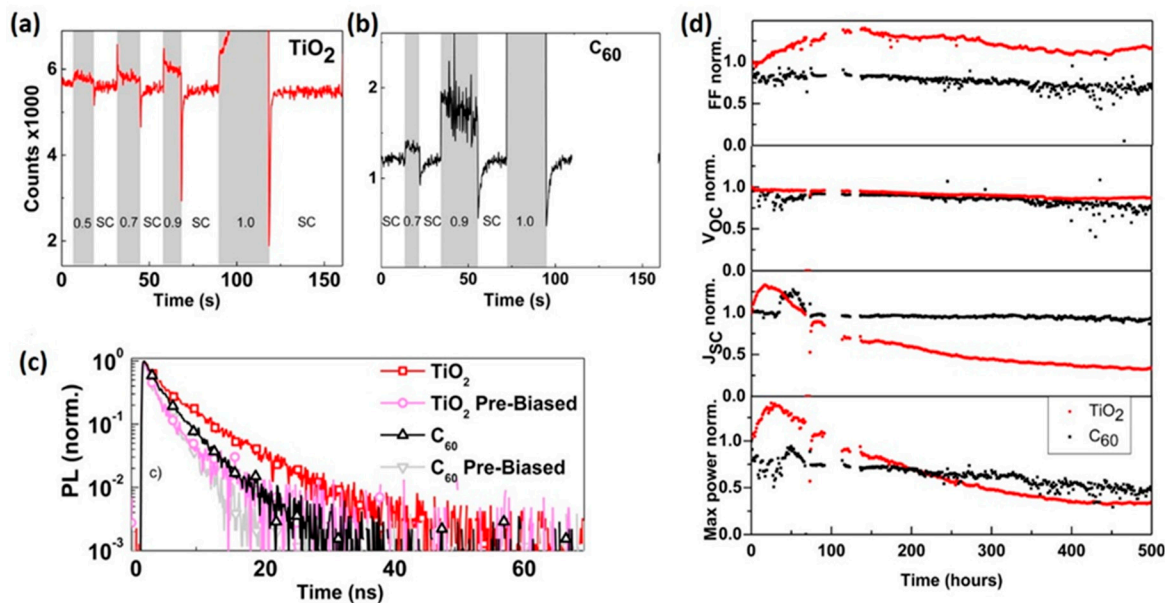


**Figure 7.** Steady state PL measured over time with (a) compact TiO<sub>2</sub> or (b) C<sub>60</sub> acceptor electron transport layers (ETLs) at short circuit and different forward biases. (c) Time resolved PL decays for the devices before and after applying 1 V forward bias. The pre-biased devices are measured within 3 s after applying the forward bias. (d) Photovoltaic parameters extracted from J-V curves for both cells after heat treatment at 60 °C for 500 h. J-V curves were measured every 65 min. Reprinted with permission from [53]. Copyright (2015) American Chemical Society.

#### 4.2. Hole Transport Layers

The most commonly used hole transport layer in inverted perovskite device structure is poly(3,4-ethylenedioxythiophene) polystyrene sulfonate (PEDOT:PSS). However, the prime disadvantage of the PEDOT:PSS based hole transport layer (HTL) is that it leads to the chemical instability of perovskite solar devices due to its acidity and highly hygroscopic nature [54–56]. Vitoratos et al. [57] investigated the thermal stability of PEDOT:PSS and found a decrease in the electrical conductivity of perovskites with aging due to the shrinkage of PEDOT conductive grains. Moreover, the XPS and UPS measurements suggested a broken conformational PEDOT:PSS structure, which results in the thermal instability of this material [57]. Despite this, a recent study [58] showed the potential for improved efficiency and stability of perovskite solar cells with enhanced PEDOT:PSS HTLs. This was done by fabricating PEDOT:PSS monolayers, using spin coating and ultrapure water rinse, and constructing ultra-thin layer of PEDOT:PSS. The water rinsed device sustained more than 50% of its stability, attributed to the less hygroscopic nature of the thin PEDOT:PSS layer [58]. Another improvement approach is to use an oxide-based hole transporting material such as NiO, which exhibits better air [59–61] and thermal stability [62].

Xu et al. [63] synthesized cross-linked films using an arylamine derivative (N4,N4'-Di(naphthalen-1-yl)-N4,N4'-bis(4-vinylphenyl)biphenyl-4,4'-diamine) (VNBP) [63]. A two-step process was employed to construct a thermally cross-linked hole extracting layer, as shown in Figure 8a. In the first step, a layer of VNBP is deposited and then thermally cross-linked; in the second step, an interface doping layer of MoO<sub>3</sub> is simply deposited on top of the HTL. The device architecture consisted of a double layer of VNBP-MoO<sub>3</sub>, and showed a steady-state efficiency of 16.5% and improved thermal stability compared to the control device. The device performance shown in Figure 8b,c indicates that the devices with cross-linked VNBP-MoO<sub>3</sub> HTL retained almost 90% of their initial performance with low

hysteresis for 1 h of annealing at 110 °C. Figure 8d illustrates the optical microscopy images of the control and cross-linked device before and after annealing. No morphological deformation was found for the cross-linked device, while the control device with spiro-OMeTAD HTL exhibited the chain-like structures which lead to irreversible degradation. The thermally cross-linked devices were found to be thermally stable for 30 days during thermal annealing at 110 °C for 1 h and high humidity exposure at 70% relative humidity, as evidenced by the XRD patterns (Figure 8e). The authors suggested that the exceptional barrier properties of cross-linked organic hole transport material with metal oxide allowed the device to maintain high performance under thermal stress for a longer period than that found in previous studies.

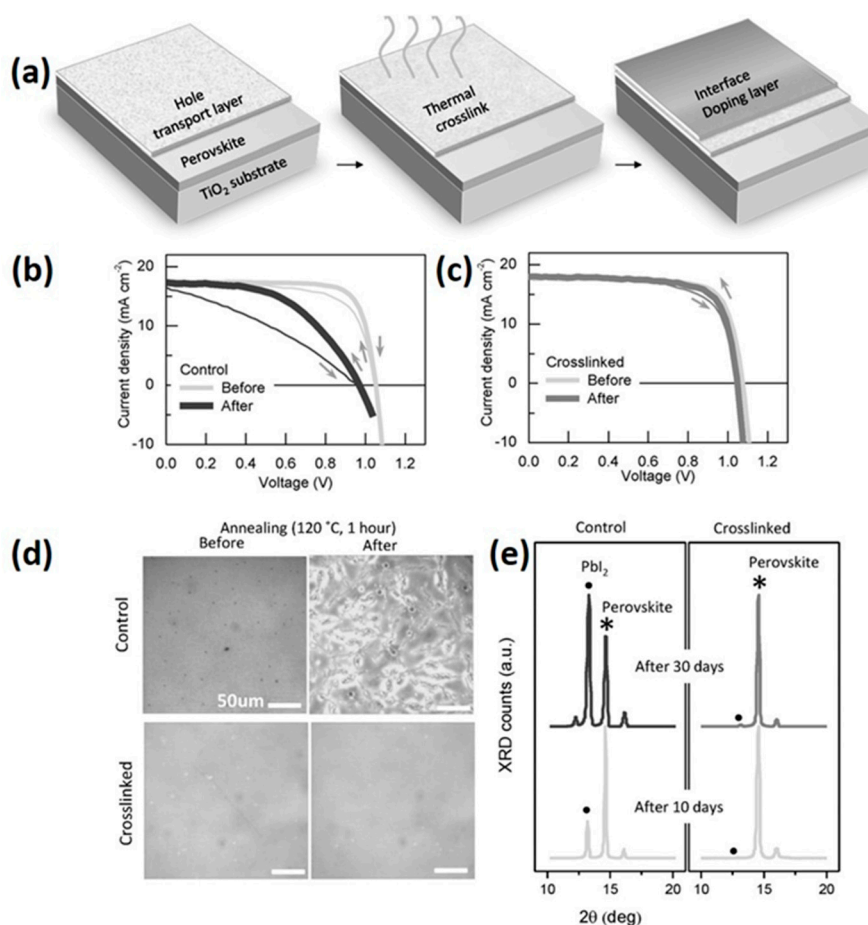


**Figure 8.** (a) Two-step process to form an insoluble and thermally stable hole extraction contact. (b) The performance of devices using Spiro-OMeTAD as the hole extraction contact tested at room temperature (light gray) and after annealing at 110 °C (dark gray). (c) The performance of devices using VNBP-MoO<sub>3</sub> tested at room temperature (light gray) and after annealing at 110 °C (dark gray). (d) Optical microscopy images of doped Spiro-OMeTAD and VNBP-MoO<sub>3</sub> films before and after annealing. (e) XRD patterns illustrating the evolution of perovskite content in the device active layer. Reprinted from [63], with permission.

Habisreutinger et al. investigated the effect of the HTL on the thermal degradation of perovskite solar cells [64]. A schematic illustration of the investigated device structure is shown in Figure 9a. The authors investigated thermal stability by employing the three most common and highly efficient HTLs, Spiro-OMeTAD, P3HT, and PTAA. A rapid degradation of the perovskite films was observed for all three HTLs, as evidenced by the photographs in Figure 9b. To achieve better thermal stability, organic HTLs were replaced with functionalized single-walled nanotubes (SWNT) embedded in an insulating polymer of polycarbonate (PC) and poly (methyl methacrylate) (PMMA). The absorption

and XRD measurements revealed that the devices with spiro-OMeTAD degraded when heated at 80 °C for 96 h in ambient environment. In contrast, devices with PMMA and PMMA-SWNT showed less degradation in absorption spectra and no significant change in the XRD patterns, as shown in Figure 9d,e. Devices fabricated with P3HT/SWNT-PMMA HTLs did not exhibit PCE reduction when annealed at 80 °C. Interestingly, the efficiency increased from 13.3% to 14.3% with an annealing time of 96 h, but a further increase in temperature led to a reduction in PCE (see Figure 9c), possibly due to the degradation of the perovskite layer at such high temperatures.

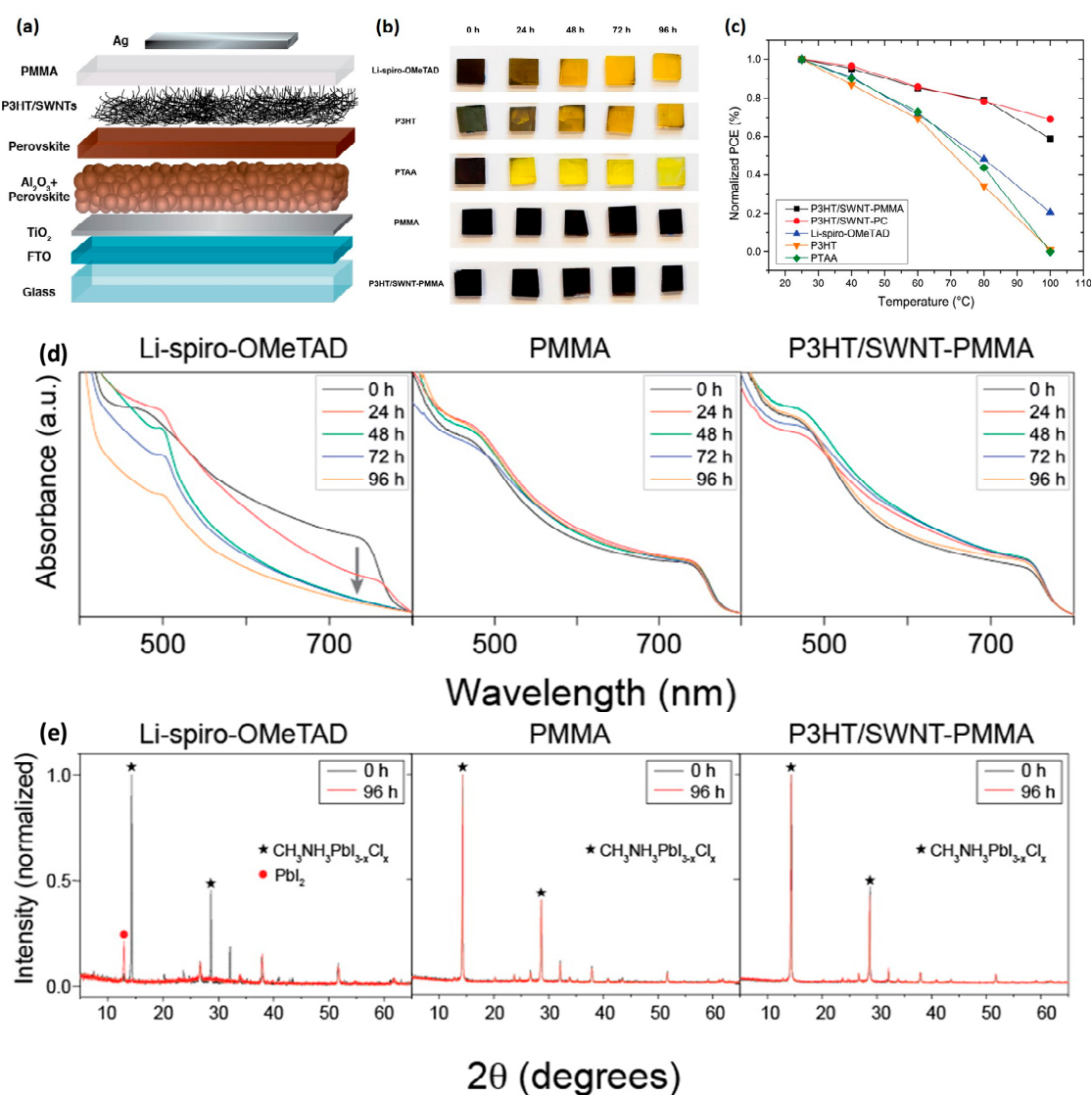


**Figure 9.** (a) Schematic of a solar cell where carbon nanotube/polymer composite is used as a hole-transport layer. (b) Photographs illustrating the visible degradation of the perovskite layer for various HTLs. (c) Temperature dependent power conversion efficiency for perovskite solar cells as a function of temperature for different HTLs. (d) Absorption measurements and (e) XRD patterns of sample with different HTLs before and after annealing for 96 h. Reprinted with permission from [64]. Copyright (2014) American Chemical Society. PMMA: poly (methyl methacrylate); SWNT: single-walled nanotubes.

#### 4.3. Metal Contacts

The most commonly used electrodes for high efficiency perovskite solar devices are gold (Au) or silver (Ag) [65–67]. Gold is expensive and can be typically replaced by Ag as an electrode in perovskite

solar cells [18,68], but both Ag and Au layers show degradation when exposed to thermal stress [69,70]. Domanski et al. reported the migration of gold through HTL into the perovskite materials at 70 °C [70]. Li et al. showed, in an inverted perovskite solar cell, that ions migrating from MAPbI<sub>3</sub> thin film diffused through the Phenyl-C61-butyric acid methyl ester (PCBM) ETL and accumulated at the Ag surface in N<sub>2</sub> at 85 °C [71]. The proposed mechanism of the Ag-electrode induced thermal degradation of the inverted PSCs is shown in Figure 10a. The loss of methylammonium iodide (MAI) occurred at the grain boundaries (GBs), and upon thermal annealing, the AgI, MA<sup>+</sup>, and I<sup>-</sup> ions migrate to reconstruct the GBs, creating more defects in the bulk grains and at the MAPbI<sub>3</sub>/PCBM interface. Multiple reports have investigated an alternative to Au and Ag based electrodes by employing carbon as a back-contact material [16,72]. Li et al. [16] fabricated a hole-conductor-free PSC based on a triple layer architecture with printed carbon electrode. The triple layer consists of mesoporous TiO<sub>2</sub> and ZrO<sub>2</sub>, as well as a 10 μm thick carbon layer. A schematic is shown in Figure 10b. The perovskite precursor solution was infiltrated by drop casting using a carbon counter electrode. The fabricated perovskite was (5-AVA)<sub>x</sub>(MA)<sub>1-x</sub>PbI<sub>3</sub>, where 5-AVA is 5-ammoniumvaleric acid iodide. The device structure displayed excellent stability and an encapsulated device showed stable performance during outdoor operation for seven consecutive days (Figure 10c) in Jeddah, Saudi Arabia [16]. Moreover, the encapsulated device remained thermally stable when annealed at 80–85 °C for 90 days, in the dark. Hence, the use of carbon as a back-contact can be beneficial to make stable PSCs at a temperature of 100 °C, representing progress toward the commercialization of PSCs [73]. Baranwal et al. [73] also fabricated a three-layer printable HTL-free MAPbI<sub>3</sub> PSC with a mesoporous carbon back contact and UV-curable sealant and performed thermal stability tests of over 1500 h at 100 °C. Interestingly, they found that the position of the UV-curing glue considerably affected device stability. The PCE of side-sealed devices (Figure 10e) remained almost constant during the thermal test over 1500 h (Figure 10f), while for the over-sealed device (Figure 10d), the PCE deteriorated to 20% of the initial value during the 100 °C thermal stress test after only 30 h.

## 5. Other Strategies to Improve Thermal Stability

Several techniques can be used to achieve thermally stable perovskite solar cells. Manipulating the electron and hole transport layers and metal contacts as discussed extensively in the previous section is one approach. Here, we describe complementary technologies that researchers have adopted to improve the thermal stability of perovskite solar cells.

Yun et al. [74] showed that the thermal stability of perovskite solar cells can be improved by constructing 2D/3D stacking structures. 2D perovskite materials exhibit better moisture stability than 3D perovskite materials [75–79], but the highest efficiency of 2D perovskite solar cells reported in literature is relatively low [80]. Yun et al. fabricated a thin layer of 2D perovskite on top of 3D perovskites in order to cover the surface and grain boundaries. Since the grain boundaries of the perovskite are defective and degradation occurs at the grain boundaries [81], covering the crystal boundaries of the 3D structure by the 2D stacking structure improves overall device stability and maintains high efficiency. They constructed 2D/3D stacking structures by reacting n-butylamine (BA) with the surface of 3D perovskites (see Figure 11a–c). Two types of solutions were used to investigate the thermal stability: BA dissolved in chlorobenzene and n-butylamine iodide (BAI) dissolved in isopropyl alcohol. The SEM images (Figure 11d–f) revealed that the BA solution spun-coated on top of the 3D perovskite layers enhanced the surface smoothness due to the gradual diffusion of BA molecules into the perovskite crystal structure, passivating surface and grain boundaries. The BAI treated film exhibited a relatively rougher surface morphology (Figure 11f), which was attributed to 3D to 2D phase transition [82]. The thermal stress studies using capacitance versus frequency measurements showed that when the device was annealed at 85 °C for 20 h, the device based on the 3D structure had a capacitance greater than that of the fresh perovskite in the low-frequency regime. This high capacitance in the low-frequency regime was attributed to ionic migration at moderately high temperature [8,83,84]. The modified perovskite film also showed better thermal stability under continuous annealing for

1000 h compared to the fresh perovskite, with the modified devices maintaining 96.5% and 88.2% of their initial efficiencies for devices with BA and BAI treatments, respectively, while the fresh device degraded to 69.8% of its initial efficiency under thermal stress [74].

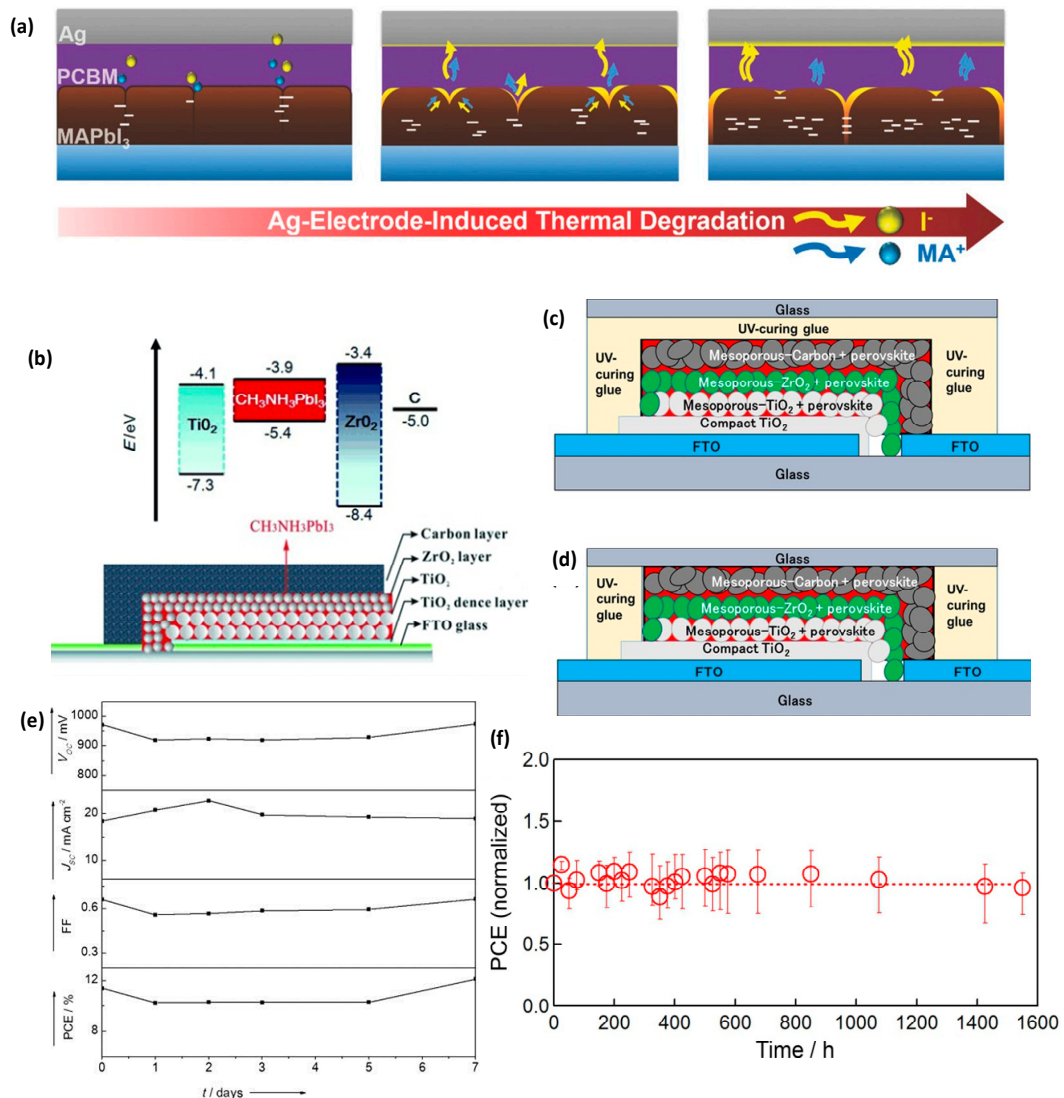


**Figure 10.** (a) A proposed mechanism for Ag-electrode-induced thermal degradation of the inverted perovskite solar cells (PSCs). Reprinted from [71], with permission. (b) A schematic of fabricated perovskite solar cells (PSCs) with carbon electrodes and (c) Photovoltaic parameters of the encapsulated perovskite solar cell plotted versus time during outdoor aging in Jeddah, Saudi Arabia. Reprinted from [16], with permission. Diagram of a three-layer perovskite device: (d) over-sealed and (e) side-sealed cell. (f) photo-conversion efficiency (PCE) of PSCs fabricated using the side-sealing configuration during thermal stability testing at different temperatures in the dark. Reprinted from [73], with permission.

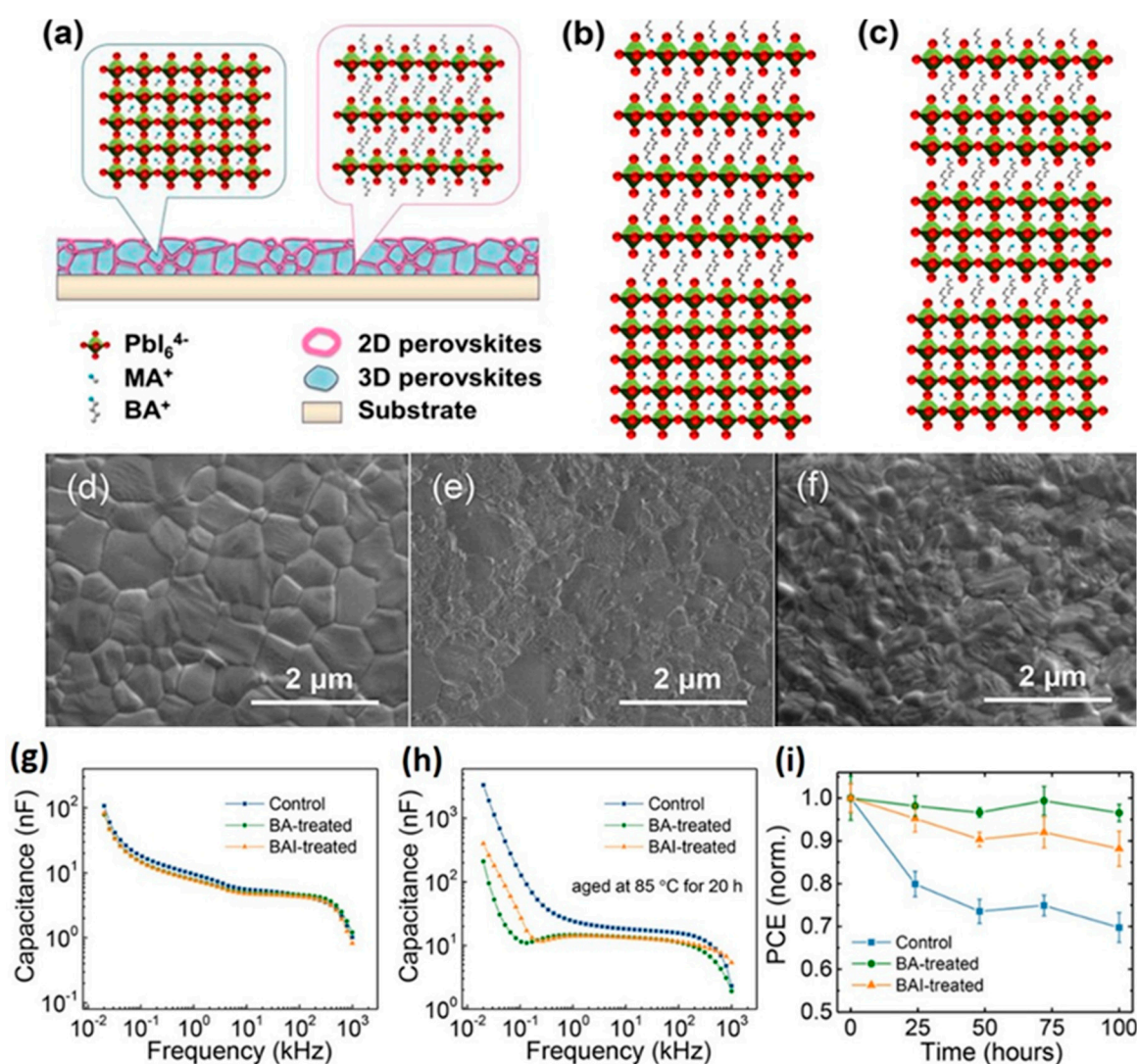


**Figure 11.** (a) A schematic of 2D/3D stacking structure obtained from BA-treated perovskite film. (b,c) 2D/3D molecular junctions on the surface and at grain boundaries of 3D perovskite films with BA and BAI treatments, respectively. SEM images of (d) MAPbI<sub>3</sub> films, (e) BA-treated MAPbI<sub>3</sub> films, and (f) BAI-treated MAPbI<sub>3</sub> films. Capacitance–frequency spectra (g) before and (h) after thermal stress at 85 °C for 20 h of the control, BA-treated, and BAI-treated devices; (i) Time evolution of normalized PCE under thermal stress. Reprinted with permission from [74]. Copyright (2018) American Chemical Society.

Li et al. investigated the thermal stability of MAPbI<sub>3</sub> by modifying its surface. In that study, an additive butylphosphonic acid 4-ammoniumchloride (4-ABPACl) was spun-coated onto the surface [16]. Structural, morphological, and elemental examinations then showed that the additive acted as a crosslink between perovskite grains. The phosphonic acid ammonium additive facilitated obtaining a smooth surface layer because perovskite was incorporated into the mesoporous TiO<sub>2</sub> scaffold. The 4-ABPACl additive increased the absorption and almost doubled the efficiency of the devices, compared to the control device. The effect of thermal stress was investigated on an encapsulated device at 45 °C under 10 mW/cm<sup>2</sup> illumination. The CH<sub>3</sub>NH<sub>3</sub>PbI<sub>3</sub>-ABPA modified devices maintained 90% of their initial efficiency after one week. A heat stress test was performed on CH<sub>3</sub>NH<sub>3</sub>PbI<sub>3</sub>-ABPA device at 85 °C in the dark for 350 h to confirm if the modified device could endure the exposure to high temperature and the modified device maintained 80% of its initial PCE after 350 h of continuous annealing.

Perovskite thin films are very sensitive to oxygen and moisture, even though different cations and mixed halides have been employed in perovskite structures. Moisture ingress is known to accelerate the thermal degradation of perovskite solar cells, so encapsulation is used to protect perovskites from moisture. Matteocci et al. [85] compared five different glass-glass sealing procedures and found an optimized procedure using Kapton and glue bonded glass. They also showed that an additional edge sealing increased moisture resistance, leading to improved thermal stability with the ability to maintain initial PCE for over 1300 h of shelf-life. Furthermore, they found that the optimized sealing procedure prevents the intrinsic degradation of  $\text{CH}_3\text{NH}_3\text{PbI}_3$ , although a reduction in PCE of 0.1%/h at 60 °C and 0.21% at 85 °C was also observed. They suggested that this reduction was attributed to the degradation of Spiro-OMeTAD HTL. A different sealing procedure approach can include the use of polymers such as poly(methyl methacrylate) (PMMA), polycarbonate (PC), or polystyrene to protect perovskite films from oxygen and moisture [64]. Along with protection from air, polymers act as an insulating tunneling contact and passivate defects in perovskite film by increasing the efficiency by more than 18% [86]. Habisreutinger et al. proposed a device architecture consisting of single-walled carbon nanotubes (SWNTs) and a polymer matrix of PMMA or PC. The SWNTs in such architecture facilitate selective charge extraction, while the polymer matrix serves as an encapsulating layer to protect the device from moisture penetration [64]. The proposed devices showed enhanced thermal stability at high temperatures of 80 °C in ambient humidity conditions, compared to the control devices.

Another approach to improve thermal stability is substituting the methylammonium (MA) cation of the perovskite material, with mixed cation-based perovskites having been extensively studied by researchers. Enhanced crystallinity and structural stability with improved power conversion efficiency were obtained by replacing MA with formamidinium (FA) [87–89], cesium (Cs) cations, [90–93] or a mixture of the two [94–98]. Eperon et al. reported a relatively slower degradation for  $\text{FAPbI}_3$  compared to  $\text{MAPbI}_3$  when annealed at 150 °C [89]. Although  $\text{FAPbI}_3$  is more thermally stable than  $\text{MAPbI}_3$ , the structural instability of  $\text{FAPbI}_3$  in the presence of moisture limits its use in perovskite solar devices [99]. Replacing FAI by MAI or MABr results in  $\text{FA}_{1-x}\text{MA}_x\text{PbI}_3$  or  $\text{FA}_{1-x}\text{MA}_x\text{PbI}_{3-y}\text{Br}_y$  perovskites, with a stabilized black perovskite phase [87,88]. Binek et al. achieved 3D black FA-based perovskite by adding a smaller MA cation compared to FA, resulting in no phase transition in the 25–150 °C temperature range [98]. Such stability improvement was ascribed to the larger dipole moment of MA, which increases the Coulomb interactions within the structure [98].

However, since the unstable nature of the MA cation can hinder long-term stability, inorganic cations, such as cesium, have attracted on-going research attention due to their established sustainability at higher temperatures [90–93]. For example,  $\text{CsPbI}_3$  based perovskite forms in a cubic structure with a band gap of 1.73 eV [89,90]. but crystallizes into a photo-inactive yellow phase when exposed to air. In contrast,  $\text{CsPbBr}_3$  is less sensitive to moisture [92,100], but does not have a favorable bandgap for single-junction solar cell applications [101]. Since inorganic cesium lead halide perovskites ( $\text{CsPbX}_3$ , X = Cl, Br, I) have demonstrated advantageous thermal stability, efforts have been made to develop mixed cation perovskites with simultaneous high efficiency and good thermal stability [28,94–96,102]. Several groups have studied Cs/FA mixtures, showing enhanced stability results in light, moisture, and heat compared to the pure material ( $\text{FAPbI}_3$ ). Saliba et al. have also fabricated solar cells using quadruple-cation perovskites (MA/FA/Cs/Rb), revealing improved reproducibility and stability [103]. Saliba et al. tested devices annealed for 500 h at 85 °C under continuous illumination in a nitrogen atmosphere, and the current-voltage characteristics of the best performance solar cells and the external quantum efficiency (EQE) electroluminescence (EL) are shown in Figure 12a–c, where the compounded stress test exceeds industrial standards [104]. They showed that the device retained 95% of its initial performance when annealed at 85 °C for 500 h, as shown in Figure 12d.

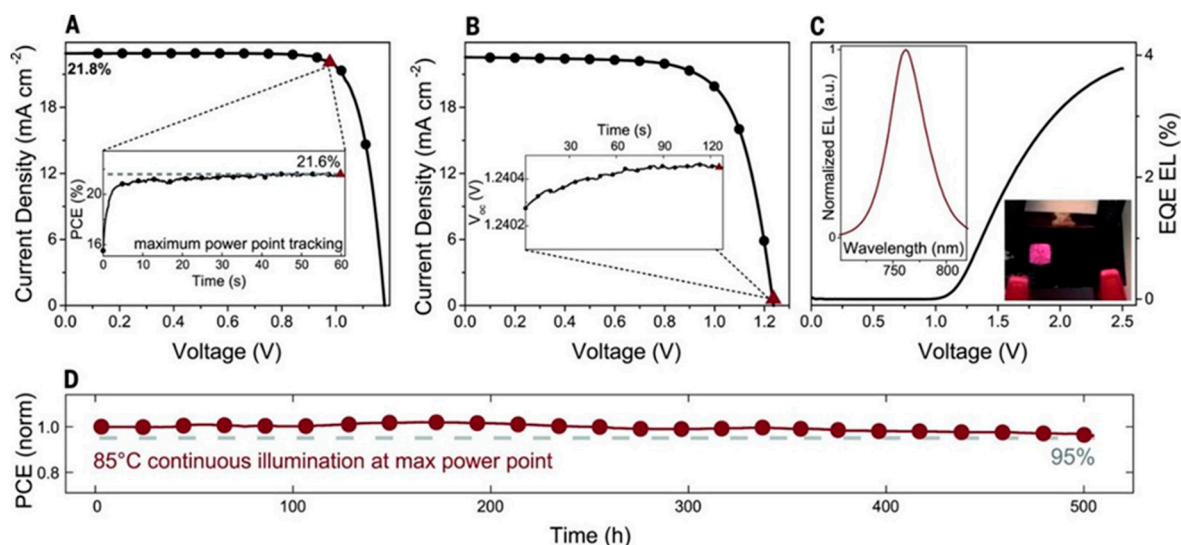


**Figure 12.** (a) Current density–voltage (J–V) curve of the highest performance RbCsMAFA solar cell. The inset shows the scan rate–independent maximum power point (MPP) tracking for 60 s. (b) J–V curve of the highest- $V_{OC}$  device. The inset illustrates the  $V_{OC}$  for 120 s (c) EQE electroluminescence (EL) versus voltage. The left and right inset show the corresponding EL spectrum and two areas of a solar cell, respectively (d) Thermal stability as a function of time for the perovskite solar cell. Reprinted with permission from [103].

## 6. Conclusions

Organic-inorganic halide perovskites have been extensively used in solar cells as a promising light harvesting material due to their excellent optoelectronic properties. Although perovskite solar cells have achieved photo-conversion efficiencies above 20%, the instability of their materials at elevated temperatures is a major issue that needs to be solved for commercial use. Particularly, perovskite films tend to exhibit intrinsic thermal degradation mechanisms under thermal stress. Typically, the commonly used  $\text{MAPbI}_3$  perovskite material is decomposed into MAI and  $\text{PbI}_2$  at elevated temperatures. The decomposition of perovskites has been discussed here from the chemical, morphological, and optical points of view, confirming the deterioration of perovskites during thermal stress. Furthermore, since perovskite solar devices are composed of many layers, notably an electron transport layer, a hole transport layer, and electrodes, other decomposition challenges exist. Thus, to facilitate better thermal stability, the selective incorporation of electron and hole transport layers and the replacement of silver or gold electrodes is discussed, and the enhancement of the stability of the perovskite layer by encapsulation or including additives is also reviewed. Currently, perovskite solar cells have been made thermally stable for annealing of up to 500 h at 85 °C by using quadruple-cation perovskites, but with available solar products on the market (c-Si, CdTe, CIGS, GaAs) guaranteed to remain stable for up to 25 years, perovskites continue to need research attention. Recent advances in perovskite solar cell thermal stability and in determining the causes of degradation indicate that it should be possible to achieve similar longevity, and support the scalable solutions that would allow this promising technology to reach its full potential and compete in the existing solar market.

**Author Contributions:** Authors equally contributed to the review paper.

**Funding:** This research was partially supported by the National Science Foundation under projects (1355678 and 1547771) and the Virginia Microelectronic Consortium Program.

**Conflicts of Interest:** The authors declare no conflict of interest.

## References

1. Wright, M.; Uddin, A. Organic–Inorganic hybrid solar cells: A comparative review. *Sol. Energy Mater Sol. Cells* **2012**, *107*, 87–111. [CrossRef]
2. NREL Solar Cell Efficiency Chart. Available online: <http://www.nrel.gov/ncpv/> (accessed on 9 September 2018).
3. Kojima, A.; Teshima, K.; Shirai, Y.; Miyasaka, T. Organometal halide perovskites as visible-light sensitizers for photovoltaic cells. *J. Am. Chem. Soc.* **2009**, *131*, 6050–6051. [CrossRef] [PubMed]
4. Lee, M.M.; Teuscher, J.; Miyasaka, T.; Murakami, T.N.; Snaith, H.J. Efficient hybrid solar cells based on meso-superstructured organometal halide perovskites. *Science* **2012**, 1228604. [CrossRef] [PubMed]
5. Wojciechowski, K.; Saliba, M.; Leijtens, T.; Abate, A.; Snaith, H.J. Sub-150 °C processed meso-superstructured perovskite solar cells with enhanced efficiency. *Energy Environ. Sci.* **2014**, *7*, 1142–1147. [CrossRef]
6. Berhe, T.A.; Su, W.N.; Chen, C.H.; Pan, C.J.; Cheng, J.H.; Chen, H.M.; Tsai, M.C.; Chen, L.Y.; Dubale, A.A.; Hwang, B.J. Organometal halide perovskite solar cells: Degradation and stability. *Energy Environ. Sci.* **2016**, *9*, 323–356. [CrossRef]
7. Hao, F.; Stoumpos, C.C.; Cao, D.H.; Chang, R.P.; Kanatzidis, M.G. Lead-free solid-state organic–inorganic halide perovskite solar cells. *Nat. Photonics* **2014**, *8*, 489. [CrossRef]
8. Lin, Q.; Armin, A.; Nagiri, R.C.R.; Burn, P.L.; Meredith, P. Electro-optics of perovskite solar cells. *Nat. Photonics* **2015**, *9*, 106. [CrossRef]
9. Miyata, A.; Mitioglu, A.; Plochocka, P.; Portugall, O.; Wang, J.T.W.; Stranks, S.D.; Snaith, H.J.; Nicholas, R.J. Direct measurement of the exciton binding energy and effective masses for charge carriers in organic-inorganic tri-halide perovskites. *Nat. Phys.* **2015**, *11*, 582–587. [CrossRef]
10. Stranks, S.D.; Eperon, G.E.; Grancini, G.; Menelaou, C.; Alcocer, M.J.; Leijtens, T.; Herz, L.M.; Petrozza, A.; Snaith, H.J. Electron-hole diffusion lengths exceeding 1 micrometer in an organometal trihalide perovskite absorber. *Science* **2013**, *342*, 341–344. [CrossRef]
11. Xing, G.; Mathews, N.; Sun, S.; Lim, S.S.; Lam, Y.M.; Grätzel, M.; Mhaisalkar, S.; Sum, T.C. Long-range balanced electron-and hole-transport lengths in organic-inorganic CH<sub>3</sub>NH<sub>3</sub>PbI<sub>3</sub>. *Science* **2013**, *342*, 344–347. [CrossRef]
12. Noh, J.H.; Im, S.H.; Heo, J.H.; Mandal, T.N.; Seok, S.I. Chemical management for colorful, efficient, and stable inorganic–organic hybrid nanostructured solar cells. *Nano Lett.* **2013**, *13*, 1764–1769. [CrossRef] [PubMed]
13. Wang, D.; Wright, M.; Elumalai, N.K.; Uddin, A. Stability of perovskite solar cells. *Sol. Energy Mater Sol. Cells* **2016**, *147*, 255–275. [CrossRef]
14. Niu, G.; Guo, X.; Wang, L. Review of recent progress in chemical stability of perovskite solar cells. *J. Mater. Chem. A* **2015**, *3*, 8970–8980. [CrossRef]
15. Grätzel, M. The light and shade of perovskite solar cells. *Nat. Mater.* **2014**, *13*, 838. [CrossRef] [PubMed]
16. Li, X.; Tschumi, M.; Han, H.; Babkair, S.S.; Alzubaydi, R.A.; Ansari, A.A.; Habib, S.S.; Nazeeruddin, M.K.; Zakeeruddin, S.M.; Grätzel, M. Outdoor performance and stability under elevated temperatures and long-term light soaking of triple-layer mesoporous perovskite photovoltaics. *Energy Technol.* **2015**, *3*, 551–555. [CrossRef]
17. Han, Y.; Meyer, S.; Dkhissi, Y.; Weber, K.; Pringle, J.M.; Bach, U.; Spiccia, L.; Cheng, Y.B. Degradation observations of encapsulated planar CH<sub>3</sub>NH<sub>3</sub>PbI<sub>3</sub> perovskite solar cells at high temperatures and humidity. *J. Mater. Chem. A* **2015**, *3*, 8139–8147. [CrossRef]
18. Leijtens, T.; Eperon, G.E.; Pathak, S.; Abate, A.; Lee, M.M.; Snaith, H.J. Overcoming ultraviolet light instability of sensitized TiO<sub>2</sub> with meso-superstructured organometal tri-halide perovskite solar cells. *Nat. Commun.* **2013**, *4*, 2885. [CrossRef]
19. Chen, W.; Wu, Y.; Yue, Y.; Liu, J.; Zhang, W.; Yang, X.; Chen, H.; Bi, E.; Ashraful, I.; Grätzel, M.; et al. Efficient and stable large-area perovskite solar cells with inorganic charge extraction layers. *Science* **2015**, aad1015. [CrossRef]
20. Shao, Y.; Yuan, Y.; Huang, J. Correlation of energy disorder and open-circuit voltage in hybrid perovskite solar cells. *Nat. Energy* **2016**, *1*, 15001. [CrossRef]
21. Cheacharoen, R.; Boyd, C.C.; Burkhard, G.F.; Leijtens, T.; Raiford, J.A.; Bush, K.A.; Bent, S.F.; McGehee, M.D. Encapsulating perovskite solar cells to withstand damp heat and thermal cycling. *Sustain. Energy Fuels* **2018**, *2*, 2398–2406. [CrossRef]

22. Leijtens, T.; Eperon, G.E.; Noel, N.K.; Habisreutinger, S.N.; Petrozza, A.; Snaith, H.J. Stability of metal halide perovskite solar cells. *Adv. Energy Mater.* **2015**, *5*, 1500963. [[CrossRef](#)]
23. Chen, Q.; De Marco, N.; Yang, Y.M.; Song, T.B.; Chen, C.C.; Zhao, H.; Hong, Z.; Zhou, H.; Yang, Y. Under the spotlight: The organic–inorganic hybrid halide perovskite for optoelectronic applications. *Nano Today* **2015**, *10*, 355–396. [[CrossRef](#)]
24. Goldschmidt, V.M. Krystallbau und chemische Zusammensetzung. *Ber. Dtsch. Chem.* **1927**, *60*, 1263–1296. [[CrossRef](#)]
25. Leijtens, T.; Bush, K.; Cheacharoen, R.; Beal, R.; Bowring, A.; McGehee, M.D. Towards enabling stable lead halide perovskite solar cells; interplay between structural, environmental, and thermal stability. *J. Mater. Chem. A* **2017**, *5*, 11483–11500. [[CrossRef](#)]
26. Li, C.; Lu, X.; Ding, W.; Feng, L.; Gao, Y.; Guo, Z. Formability of ABX<sub>3</sub> (X=F, Cl, Br, I) Halide Perovskites. *Acta Crystallogr. B* **2008**, *64*, 702–707. [[CrossRef](#)] [[PubMed](#)]
27. Bakulin, A.A.; Selig, O.; Bakker, H.J.; Rezus, Y.L.; Muller, C.; Glaser, T.; Lovrincic, R.; Sun, Z.; Chen, Z.; Walsh, A.; et al. Real-Time Observation of Organic Cation Reorientation in Methylammonium Lead Iodide Perovskites. *J. Phys. Chem. Lett.* **2015**, *6*, 3663–3669. [[CrossRef](#)] [[PubMed](#)]
28. Li, Z.; Yang, M.; Park, J.S.; Wei, S.H.; Berry, J.J.; Zhu, K. Stabilizing perovskite structures by tuning tolerance factor: Formation of formamidinium and cesium lead iodide solid-state alloys. *Chem. Mater.* **2015**, *28*, 284–292. [[CrossRef](#)]
29. Lee, J.; Seol, D.; Cho, A.; Park, N. High-Efficiency Perovskite Solar Cells Based on the Black Polymorph of HC(NH<sub>2</sub>)<sub>2</sub>PbI<sub>3</sub>. *Adv. Mater.* **2014**, *26*, 4991–4998. [[CrossRef](#)]
30. Chang, Y.H.; Park, C.H.; Matsuishi, K. First-Principles Study of the Structural and the Electronic Properties of the Lead-Halide-Based Inorganic–Organic Perovskites (CH<sub>3</sub>NH<sub>3</sub>)PbX<sub>3</sub> and CsPbX<sub>3</sub> (X=Cl, Br, I). *J. Korean Phys. Soc.* **2004**, *44*, 889–893.
31. Umari, P.; Mosconi, E.; De Angelis, F. Relativistic GW calculations on CH<sub>3</sub>NH<sub>3</sub>PbI<sub>3</sub> and CH<sub>3</sub>NH<sub>3</sub>SnI<sub>3</sub> perovskites for solar cell applications. *Sci. Rep.* **2014**, *4*, 4467. [[CrossRef](#)]
32. Umebayashi, T.; Asai, K.; Kondo, T.; Nakao, A. Electronic structures of lead iodide based low-dimensional crystals. *Phys. Rev. B* **2003**, *67*, 155405. [[CrossRef](#)]
33. Wasylishen, R.E.; Knop, O.; Macdonald, J.B. Cation rotation in methylammonium lead halides. *Solid State Commun.* **1985**, *56*, 581–582. [[CrossRef](#)]
34. Egger, D.A.; Kronik, L.; Rappe, A.M. Theory of hydrogen migration in organic–inorganic halide perovskites. *Angew. Chem. Int. Ed.* **2015**, *54*, 12437–12441. [[CrossRef](#)] [[PubMed](#)]
35. Ball, J.M.; Lee, M.M.; Hey, A.; Snaith, H.J. Low-temperature processed meso-superstructured to thin-film perovskite solar cells. *Energy Environ. Sci.* **2013**, *6*, 1739–1743. [[CrossRef](#)]
36. Stoumpos, C.C.; Malliakas, C.D.; Kanatzidis, M.G. Semiconducting tin and lead iodide perovskites with organic cations: Phase transitions, high mobilities, and near-infrared photoluminescent properties. *Inorg. Chem.* **2013**, *52*, 9019–9038. [[CrossRef](#)]
37. Im, J.H.; Lee, C.R.; Lee, J.W.; Park, S.W.; Park, N.G. 6.5% efficient perovskite quantum-dot-sensitized solar cell. *Nanoscale* **2011**, *3*, 4088–4093. [[CrossRef](#)] [[PubMed](#)]
38. Conings, B.; Drijkoningen, J.; Gauquelin, N.; Babayigit, A.; D’Haen, J.; D’Olieslaeger, L.; Ethirajan, A.; Verbeeck, J.; Manca, J.; Mosconi, E.; et al. Intrinsic thermal instability of methylammonium lead trihalide perovskite. *Adv. Energy Mater.* **2015**, *5*, 1500477. [[CrossRef](#)]
39. Juarez-Perez, E.J.; Hawash, Z.; Raga, S.R.; Ono, L.K.; Qi, Y. Thermal degradation of CH<sub>3</sub>NH<sub>3</sub>PbI<sub>3</sub> perovskite into NH<sub>3</sub> and CH<sub>3</sub>I gases observed by coupled thermogravimetry–mass spectrometry analysis. *Energy Environ. Sci.* **2016**, *9*, 3406–3410. [[CrossRef](#)]
40. Fan, Z.; Xiao, H.; Wang, Y.; Zhao, Z.; Lin, Z.; Cheng, H.C.; Lee, S.J.; Wang, G.; Feng, Z.; Goddard, W.A., III; et al. Layer-by-layer degradation of methylammonium lead tri-iodide perovskite microplates. *Joule* **2017**, *1*, 548–562. [[CrossRef](#)]
41. Pauling, L. The dependence of bond energy on bond length. *J. Phys. Chem.* **1954**, *58*, 662–666. [[CrossRef](#)]
42. Frost, J.M.; Butler, K.T.; Brivio, F.; Hendon, C.H.; Van Schilfegaarde, M.; Walsh, A. Atomistic origins of high-performance in hybrid halide perovskite solar cells. *Nano Lett.* **2014**, *14*, 2584–2590. [[CrossRef](#)] [[PubMed](#)]

43. Christians, J.A.; Miranda Herrera, P.A.; Kamat, P.V. Transformation of the excited state and photovoltaic efficiency of  $\text{CH}_3\text{NH}_3\text{PbI}_3$  perovskite upon controlled exposure to humidified air. *J. Am. Chem. Soc.* **2015**, *137*, 1530–1538. [[CrossRef](#)] [[PubMed](#)]
44. Yang, J.; Siempelkamp, B.D.; Liu, D.; Kelly, T.L. Investigation of  $\text{CH}_3\text{NH}_3\text{PbI}_3$  degradation rates and mechanisms in controlled humidity environments using in situ techniques. *ACS Nano* **2015**, *9*, 1955–1963. [[CrossRef](#)] [[PubMed](#)]
45. Smecca, E.; Numata, Y.; Deretzis, I.; Pellegrino, G.; Boninelli, S.; Miyasaka, T.; La Magna, A.; Alberti, A. Stability of solution-processed  $\text{MAPbI}_3$  and  $\text{FAPbI}_3$  layers. *Phys. Chem. Chem. Phys.* **2016**, *18*, 13413–13422. [[CrossRef](#)] [[PubMed](#)]
46. Philippe, B.; Park, B.W.; Lindblad, R.; Oscarsson, J.; Ahmadi, S.; Johansson, E.M.; Rensmo, H. Chemical and Electronic Structure Characterization of Lead Halide Perovskites and Stability Behavior under Different Exposures-A Photoelectron Spectroscopy Investigation. *Chem. Mater.* **2015**, *27*, 1720–1731. [[CrossRef](#)]
47. Foley, B.J.; Marlowe, D.L.; Sun, K.; Saidi, W.A.; Scudiero, L.; Gupta, M.C.; Choi, J.J. Temperature dependent energy levels of methylammonium lead iodide perovskite. *Appl. Phys. Lett.* **2015**, *106*, 243904. [[CrossRef](#)]
48. Al Mamun, A.; Ava, T.T.; Byun, H.R.; Jeong, H.J.; Jeong, M.S.; Nguyen, L.; Gausin, C.; Namkoong, G. Unveiling the irreversible performance degradation of organo-inorganic halide perovskite films and solar cells during heating and cooling processes. *Phys. Chem. Chem. Phys.* **2017**, *19*, 19487–19495. [[CrossRef](#)]
49. Milot, R.L.; Eperon, G.E.; Snaith, H.J.; Johnston, M.B.; Herz, L.M. Temperature-dependent charge-carrier dynamics in  $\text{CH}_3\text{NH}_3\text{PbI}_3$  perovskite thin films. *Adv. Funct. Mater.* **2015**, *25*, 6218–6227. [[CrossRef](#)]
50. Pathak, S.K.; Abate, A.; Ruckdeschel, P.; Roose, B.; Gödel, K.C.; Vaynzof, Y.; Santhala, A.; Watanabe, S.-I.; Hollman, D.J.; Noel, N.; et al. Performance and stability enhancement of dye-sensitized and perovskite solar cells by Al doping of  $\text{TiO}_2$ . *Adv. Funct. Mater.* **2014**, *24*, 6046–6055. [[CrossRef](#)]
51. Ahn, N.; Kwak, K.; Jang, M.S.; Yoon, H.; Lee, B.Y.; Lee, J.K.; Pikhitsa, P.V.; Byun, J.; Choi, M. Trapped charge-driven degradation of perovskite solar cells. *Nat. Commun.* **2016**, *7*, 13422. [[CrossRef](#)]
52. Wojciechowski, K.; Stranks, S.D.; Abate, A.; Sadoughi, G.; Sadhanala, A.; Kopidakis, N.; Rumbles, G.; Li, C.Z.; Friend, R.H.; Jen, A.K.Y.; et al. Heterojunction modification for highly efficient organic–inorganic perovskite solar cells. *ACS Nano* **2014**, *8*, 12701–12709. [[CrossRef](#)] [[PubMed](#)]
53. Wojciechowski, K.; Leijtens, T.; Siprova, S.; Schlueter, C.; Hörantner, M.T.; Wang, J.T.W.; Li, C.Z.; Jen, A.K.Y.; Lee, T.L.; Snaith, H.J. C60 as an efficient n-type compact layer in perovskite solar cells. *J. Phys. Chem. Lett.* **2015**, *6*, 2399–2405. [[CrossRef](#)] [[PubMed](#)]
54. Ye, S.; Sun, W.; Li, Y.; Yan, W.; Peng, H.; Bian, Z.; Liu, Z.; Huang, C. CuSCN-Based Inverted Planar Perovskite Solar Cell with an Average PCE of 15.6%. *Nano Lett.* **2015**, *15*, 3723–3728. [[CrossRef](#)] [[PubMed](#)]
55. Labban, A.E.; Chen, H.; Kirkus, M.; Barbe, J.; Del Gobbo, S.; Neophytou, M.; McCulloch, I. Improved Efficiency in Inverted Perovskite Solar Cells Employing a Novel Diarylamino-Substituted Molecule as PEDOT:PSS Replacement. *Adv. Energy Mater.* **2016**, 1502101. [[CrossRef](#)]
56. Lee, W.; Song, M.; Park, S.; Nam, S.; Seo, J.; Kim, H.; Kim, Y. Acidity-Controlled Conducting Polymer Films for Organic Thermoelectric Devices with Horizontal and Vertical Architectures. *Sci. Rep.* **2016**, *6*, 33795. [[CrossRef](#)]
57. Vitoratos, E.; Sakkopoulos, S.; Dalas, E.; Paliatsas, N.; Karageorgopoulos, D.; Petraki, F.; Kennou, S.; Choulis, S.A. Thermal degradation mechanisms of PEDOT: PSS. *Org. Electron.* **2009**, *10*, 61–66. [[CrossRef](#)]
58. Hu, L.; Li, M.; Yang, K.; Xiong, Z.; Yang, B.; Wang, M.; Tang, X.; Zang, Z.; Liu, X.; Li, B.; et al. PEDOT: PSS monolayers to enhance the hole extraction and stability of perovskite solar cells. *J. Mater. Chem. A* **2018**, *6*, 16583–16589. [[CrossRef](#)]
59. You, J.; Meng, L.; Song, T.-B.; Guo, T.-F.; Yang, Y.; Chang, W.-H.; Hong, Z.; Chen, H.; Zhou, H.; Chen, Q.; et al. Improved Air Stability of Perovskite Solar Cells via Solution- Processed Metal Oxide Transport Layers. *Nat. Nanotechnol.* **2015**, *11*, 75–81. [[CrossRef](#)]
60. Zhang, H.; Cheng, J.; Lin, F.; He, H.; Mao, J.; Wong, K.S.; Jen, A.K.-Y.; Choy, W.C.H. Pinhole-Free and Surface-Nanostructured NiOx Film by Room-Temperature Solution Process for High- Performance Flexible Perovskite Solar Cells with Good Stability and Reproducibility. *ACS Nano* **2016**, *10*, 1503–1511. [[CrossRef](#)]
61. Kim, H.-S.; Seo, J.-Y.; Park, N.-G. Impact of Selective Contacts on Long-Term Stability of  $\text{CH}_3\text{NH}_3\text{PbI}_3$  Perovskite Solar Cells. *J. Phys. Chem. C* **2016**, *120*, 27840–27848. [[CrossRef](#)]
62. Zhao, X.; Kim, H.S.; Seo, J.Y.; Park, N.G. Effect of selective contacts on the thermal stability of perovskite solar cells. *ACS Appl. Mater. Interfaces* **2017**, *9*, 7148–7153. [[CrossRef](#)] [[PubMed](#)]

63. Xu, J.; Voznyy, O.; Comin, R.; Gong, X.; Walters, G.; Liu, M.; Kanjanaboos, P.; Lan, X.; Sargent, E.H. Crosslinked Remote-Doped Hole-Extracting Contacts Enhance Stability under Accelerated Lifetime Testing in Perovskite Solar Cells. *Adv. Mater.* **2016**, *28*, 2807–2815. [[CrossRef](#)] [[PubMed](#)]
64. Habisreutinger, S.N.; Leijtens, T.; Eperon, G.E.; Stranks, S.D.; Nicholas, R.J.; Snaith, H.J. Carbon nanotube/polymer composites as a highly stable hole collection layer in perovskite solar cells. *Nano Lett.* **2014**, *14*, 5561–5568. [[CrossRef](#)] [[PubMed](#)]
65. Xu, J.; Buin, A.; Ip, A.H.; Li, W.; Voznyy, O.; Comin, R.; Yuan, M.; Jeon, S.; Ning, Z.; McDowell, J.J.; et al. Perovskite–fullerene hybrid materials suppress hysteresis in planar diodes. *Nat. Commun.* **2015**, *6*, 7081. [[CrossRef](#)] [[PubMed](#)]
66. Sheikh, A.D.; Bera, A.; Haque, M.A.; Rakhi, R.B.; Del Gobbo, S.; Alshareef, H.N.; Wu, T. Atmospheric effects on the photovoltaic performance of hybrid perovskite solar cells. *Sol. Energy Mater Sol. Cells* **2015**, *137*, 6–14. [[CrossRef](#)]
67. Sfyri, G.; Kumar, C.V.; Raptis, D.; Dracopoulos, V.; Lianos, P. Study of perovskite solar cells synthesized under ambient conditions and of the performance of small cell modules. *Sol. Energy Mater Sol. Cells* **2015**, *134*, 60–63. [[CrossRef](#)]
68. Wehrenfennig, C.; Eperon, G.E.; Johnston, M.B.; Snaith, H.J.; Herz, L.M. High charge carrier mobilities and lifetimes in organolead trihalide perovskites. *Adv. Mater.* **2014**, *26*, 1584–1589. [[CrossRef](#)]
69. Divitini, G.; Cacovich, S.; Matteocci, F.; Cina, L.; Di Carlo, A.; Ducati, C. In situ observation of heat-induced degradation of perovskite solar cells. *Nat. Energy*. **2016**, *1*, 15012. [[CrossRef](#)]
70. Domanski, K.; Correa-Baena, J.P.; Mine, N.; Nazeeruddin, M.K.; Abate, A.; Saliba, M.; Tress, W.; Hagfeldt, A.; Grätzel, M. Not all that glitters is gold: Metal-migration-induced degradation in perovskite solar cells. *ACS nano* **2016**, *10*, 6306–6314. [[CrossRef](#)]
71. Li, J.; Dong, Q.; Li, N.; Wang, L. Direct Evidence of Ion Diffusion for the Silver-Electrode-Induced Thermal Degradation of Inverted Perovskite Solar Cells. *Adv. Energy Mater.* **2017**, *7*, 1602922. [[CrossRef](#)]
72. Mei, A.; Li, X.; Liu, L.; Ku, Z.; Liu, T.; Rong, Y.; Xu, M.; Hu, M.; Chen, J.; Yang, Y.; et al. A hole-conductor-free, fully printable mesoscopic perovskite solar cell with high stability. *Science* **2014**, *345*, 295–298. [[CrossRef](#)] [[PubMed](#)]
73. Baranwal, A.K.; Kanaya, S.; Peiris, T.N.; Mizuta, G.; Nishina, T.; Kanda, H.; Miyasaka, T.; Segawa, H.; Ito, S. 100 °C thermal stability of printable perovskite solar cells using porous carbon counter electrodes. *ChemSusChem* **2016**, *9*, 2604–2608. [[CrossRef](#)] [[PubMed](#)]
74. Lin, Y.; Bai, Y.; Fang, Y.; Chen, Z.; Yang, S.; Zheng, X.; Tang, S.; Liu, Y.; Zhao, J.; Huang, J. Enhanced thermal stability in perovskite solar cells by assembling 2D/3D stacking structures. *J Phys Chem Lett.* **2018**, *9*, 654–658. [[CrossRef](#)] [[PubMed](#)]
75. Smith, I.C.; Hoke, E.T.; Solis-Ibarra, D.; McGehee, M.D.; Karunadasa, H.I. A Layered Hybrid Perovskite Solar-Cell Absorber with Enhanced Moisture Stability. *Angew. Chem. Int. Ed.* **2014**, *53*, 11232–11235. [[CrossRef](#)] [[PubMed](#)]
76. Cao, D.H.; Stoumpos, C.C.; Farha, O.K.; Hupp, J.T.; Kanatzidis, M.G. 2D Homologous Perovskites as Light-Absorbing Materials for Solar Cell Applications. *J. Am. Chem. Soc.* **2015**, *137*, 7843–7850. [[CrossRef](#)] [[PubMed](#)]
77. Tsai, H.; Nie, W.; Blancon, J.C.; Stoumpos, C.C.; Asadpour, R.; Harutyunyan, B.; Neukirch, A.J.; Verduzco, R.; Crochet, J.J.; Tretiak, S.; et al. High-Efficiency Two-Dimensional Ruddlesden-Popper Perovskite Solar Cells. *Nature* **2016**, *536*, 312–316. [[CrossRef](#)] [[PubMed](#)]
78. Quan, L.N.; Yuan, M.; Comin, R.; Voznyy, O.; Beauregard, E.M.; Hoogland, S.; Buin, A.; Kirmani, A.R.; Zhao, K.; Amassian, A.; et al. Ligand-stabilized reduced-dimensionality perovskites. *J. Am. Chem. Soc.* **2016**, *138*, 2649–2655. [[CrossRef](#)]
79. Yao, K.; Wang, X.; Xu, Y.-X.; Li, F.; Zhou, L. Multilayered Perovskite Materials Based on Polymeric-Ammonium Cations for Stable Large-Area Solar Cell. *Chem. Mater.* **2016**, *28*, 3131–3138. [[CrossRef](#)]
80. Zhang, X.; Ren, X.; Liu, B.; Munir, R.; Zhu, X.; Yang, D.; Li, J.; Liu, Y.; Smilgies, D.M.; Li, R.; et al. Stable high efficiency two-dimensional perovskite solar cells via cesium doping. *Energy Environ. Sci.* **2017**, *10*, 2095–2102. [[CrossRef](#)]
81. Wang, Q.; Chen, B.; Liu, Y.; Deng, Y.; Bai, Y.; Dong, Q.; Huang, J. Scaling behavior of moisture-induced grain degradation in polycrystalline hybrid perovskite thin films. *Energy Environ. Sci.* **2017**, *10*, 516–522. [[CrossRef](#)]

82. Yang, S.; Zheng, Y.C.; Hou, Y.; Chen, X.; Chen, Y.; Wang, Y.; Zhao, H.; Yang, H.G. Formation Mechanism of Freestanding  $\text{CH}_3\text{NH}_3\text{PbI}_3$  Functional Crystals: In Situ Transformation vs. Dissolution–Crystallization. *Chem. Mater.* **2014**, *26*, 6705–6710. [[CrossRef](#)]
83. Hoque, M.N.F.; Yang, M.; Li, Z.; Islam, N.; Pan, X.; Zhu, K.; Fan, Z. Polarization and Dielectric Study of Methylammonium Lead Iodide Thin Film to Reveal its Nonferroelectric Nature under Solar Cell Operating Conditions. *ACS Energy Lett.* **2016**, *1*, 142–149. [[CrossRef](#)]
84. Jonscher, A. Analysis of the Alternating Current Properties of Ionic Conductors. *J. Mater. Sci.* **1978**, *13*, 553–562. [[CrossRef](#)]
85. Matteocci, F.; Cinà, L.; Lamanna, E.; Cacovich, S.; Divitini, G.; Midgley, P.A.; Ducati, C.; Di Carlo, A. Encapsulation for long-term stability enhancement of perovskite solar cells. *Nano Energy* **2016**, *30*, 162–172. [[CrossRef](#)]
86. Wang, F.; Shimazaki, A.; Yang, F.; Kanahashi, K.; Matsuki, K.; Miyauchi, Y.; Takenobu, T.; Wakamiya, A.; Murata, Y.; Matsuda, K. Highly efficient and stable perovskite solar cells by interfacial engineering using solution-processed polymer layer. *J. Phys. Chem. C* **2017**, *121*, 1562–1568. [[CrossRef](#)]
87. Jeon, N.J.; Noh, J.H.; Yang, W.S.; Kim, Y.C.; Ryu, S.; Seo, J.; Seok, S.I. Compositional engineering of perovskite materials for high-performance solar cells. *Nature* **2015**, *517*, 476. [[CrossRef](#)]
88. Pellet, N.; Gao, P.; Gregori, G.; Yang, T.Y.; Nazeeruddin, M.K.; Maier, J.; Grätzel, M. Mixed-organic-cation Perovskite photovoltaics for enhanced solar-light harvesting. *Angew. Chem. Int.* **2014**, *126*, 3215–3221. [[CrossRef](#)]
89. Eperon, G.E.; Stranks, S.D.; Menelaou, C.; Johnston, M.B.; Herz, L.M.; Snaith, H.J. Formamidinium lead trihalide: A broadly tunable perovskite for efficient planar heterojunction solar cells. *Energy Environ. Sci.* **2014**, *7*, 982–988. [[CrossRef](#)]
90. Eperon, G.E.; Paterno, G.M.; Sutton, R.J.; Zampetti, A.; Haghighirad, A.A.; Cacialli, F.; Snaith, H.J. Inorganic cesium lead iodide perovskite solar cells. *J. Mater. Chem. A* **2015**, *3*, 19688–19695. [[CrossRef](#)]
91. Sutton, R.J.; Eperon, G.E.; Miranda, L.; Parrott, E.S.; Kamino, B.A.; Patel, J.B.; Hörantner, M.T.; Johnston, M.B.; Haghighirad, A.A.; Moore, D.T.; et al. Bandgap-tunable cesium lead halide perovskites with high thermal stability for efficient solar cells. *Adv. Energy Mater.* **2016**, *6*, 1502458. [[CrossRef](#)]
92. Kulbak, M.; Gupta, S.; Kedem, N.; Levine, I.; Bendikov, T.; Hodes, G.; Cahen, D. Cesium enhances long-term stability of lead bromide perovskite-based solar cells. *J. Phys. Chem. Lett.* **2015**, *7*, 167–172. [[CrossRef](#)] [[PubMed](#)]
93. Beal, R.E.; Slotcavage, D.J.; Leijtens, T.; Bowering, A.R.; Belisle, R.A.; Nguyen, W.H.; Burkhard, G.F.; Hoke, E.T.; McGehee, M.D. Cesium lead halide perovskites with improved stability for tandem solar cells. *J. Phys. Chem. Lett.* **2016**, *7*, 746–751. [[CrossRef](#)]
94. Saliba, M.; Matsui, T.; Seo, J.Y.; Domanski, K.; Correa-Baena, J.P.; Nazeeruddin, M.K.; Zakeeruddin, S.M.; Tress, W.; Abate, A.; Hagfeldt, A.; et al. Cesium-containing triple cation perovskite solar cells: Improved stability, reproducibility and high efficiency. *Energy Environ. Sci.* **2016**, *9*, 1989–1997. [[CrossRef](#)] [[PubMed](#)]
95. McMeekin, D.P.; Sadoughi, G.; Rehman, W.; Eperon, G.E.; Saliba, M.; Hörantner, M.T.; Haghighirad, A.; Sakai, N.; Korte, L.; Rech, B.; et al. A mixed-cation lead mixed-halide perovskite absorber for tandem solar cells. *Science* **2016**, *351*, 151–155. [[CrossRef](#)] [[PubMed](#)]
96. Lee, J.W.; Kim, D.H.; Kim, H.S.; Seo, S.W.; Cho, S.M.; Park, N.G. Formamidinium and cesium hybridization for photo- and moisture-stable perovskite solar cell. *Adv. Energy Mater.* **2015**, *5*, 1501310. [[CrossRef](#)]
97. Yi, C.; Luo, J.; Meloni, S.; Boziki, A.; Ashari-Astani, N.; Grätzel, C.; Zakeeruddin, S.M.; Röthlisberger, U.; Grätzel, M. Entropic stabilization of mixed A-cation  $\text{ABX}_3$  metal halide perovskites for high performance perovskite solar cells. *Energy Environ. Sci.* **2016**, *9*, 656–662. [[CrossRef](#)]
98. Binek, A.; Hanusch, F.C.; Docampo, P.; Bein, T. Stabilization of the trigonal high-temperature phase of formamidinium lead iodide. *J. Phys. Chem. Lett.* **2015**, *6*, 1249–1253. [[CrossRef](#)] [[PubMed](#)]
99. Koh, T.M.; Fu, K.; Fang, Y.; Chen, S.; Sum, T.C.; Mathews, N.; Mhaisalkar, S.G.; Boix, P.P.; Baikie, T. Formamidinium-containing metal-halide: An alternative material for near-IR absorption perovskite solar cells. *J. Phys. Chem. C* **2013**, *118*, 16458–16462. [[CrossRef](#)]
100. Kulbak, M.; Cahen, D.; Hodes, G. How important is the organic part of lead halide perovskite photovoltaic cells? Efficient  $\text{CsPbBr}_3$  cells. *J. Phys. Chem. Lett.* **2015**, *6*, 2452–2456. [[CrossRef](#)]

101. Stoumpos, C.C.; Malliakas, C.D.; Peters, J.A.; Liu, Z.; Sebastian, M.; Im, J.; Chasapis, T.C.; Wibowo, A.C.; Chung, D.Y.; Freeman, A.J.; et al. Crystal growth of the perovskite semiconductor CsPbBr<sub>3</sub>: A new material for high-energy radiation detection. *Cryst. Growth Des.* **2013**, *13*, 2722–2727. [[CrossRef](#)]
102. Choi, H.; Jeong, J.; Kim, H.B.; Kim, S.; Walker, B.; Kim, G.H.; Kim, J.Y. Cesium-doped methylammonium lead iodide perovskite light absorber for hybrid solar cells. *Nano Energy* **2014**, *7*, 80–85. [[CrossRef](#)]
103. Saliba, M.; Matsui, T.; Domanski, K.; Seo, J.Y.; Ummadisingu, A.; Zakeeruddin, S.M.; Correa-Baena, J.P.; Tress, W.R.; Abate, A.; Hagfeldt, A.; et al. Incorporation of rubidium cations into perovskite solar cells improves photovoltaic performance. *Science* **2016**, *354*, 206–209. [[CrossRef](#)] [[PubMed](#)]
104. Rong, Y.; Liu, L.; Mei, A.; Li, X.; Han, H. Beyond efficiency: The challenge of stability in mesoscopic perovskite solar cells. *Adv. Energy Mater.* **2015**, *5*, 1501066. [[CrossRef](#)]



© 2019 by the authors. Licensee MDPI, Basel, Switzerland. This article is an open access article distributed under the terms and conditions of the Creative Commons Attribution (CC BY) license (<http://creativecommons.org/licenses/by/4.0/>).